Mismatch repair deficiency drives malignant progression and alters the tumor immune microenvironment in glioblastoma models

Montserrat Puigdelloses Vallcorba[1], Nishant Soni[2†], Seung-Won Choi[3†#], Kavita Rawat[1,4†], Tanvi Joshi[1,4†], Sam Friedman[5], Alice Buonfiglioli[1], Angelo Angione[1], Zhihong Chen[1,6], Gonzalo Piñero[1], Gabrielle Price[1], Mehek Dedhia[1], Raina Roche[6,7], Emir Radkevich[6,7], Anne Bowcock[1], Deepti Bhatt[5], Winfried Edelmann[8], Robert Samstein[1,7,9], Timothy E. Richardson[10], Nadejda M. Tsankova[10], Alexander M. Tsankov[2,6,7], Ranjit S. Bindra[11,12], Raul Rabadan[3], Juan C. Vasquez[13], Dolores Hambardzumyan[1,4*]

[1]Departments of Oncological Sciences and Neurosurgery, The Tisch Cancer Institute, Icahn School of Medicine at Mount Sinai, New York, NY, USA

[2]Department of Genetics and Genomic Sciences, Icahn School of Medicine at Mount Sinai, New York, NY, USA.

[3] Departments of Systems Biology and Biomedical Informatics, Columbia University, New York, NY, USA

[4]Department of Neurosurgery, Perelman School of Medicine, University of Pennsylvania, Philadelphia, PA, USA

[5]Yale Center for Research Computing, Yale School of Medicine, P.O. Box 208040, HRT 134, New Haven, CT, USA.

[6]Human Immune Monitoring Center, Icahn School of Medicine at Mount Sinai, New York, NY, USA

[7] Lipschultz Precision Immunology Institute, Icahn School of Medicine at Mount Sinai, New York, NY, USA

[8]Department of Cell Biology, Albert Einstein College of Medicine, New York, NY, USA

[9]Tisch Cancer Institute, Icahn School of Medicine at Mount Sinai, New York, NY, USA.

[10]Department of Pathology, Molecular and Cell-Based Medicine, Icahn School of Medicine at Mount Sinai, New York, NY, USA

[11]Department of Pathology, Yale School of Medicine, New Haven, CT, USA.

[12]Department of Therapeutic Radiology, Yale School of Medicine, P.O. Box 208040, HRT 134, New Haven, CT, USA.

[13]Department of Pediatrics, Yale School of Medicine, New Haven, CT, USA

[†]These authors contributed equally

[#]Graduate School of Health Science and Technology, Ulsan National Institute of Science and Technology, Ulsan, South Korea.

Conflict of interest: The authors have declared that no conflict of interest exists.

*Correspondence to: Dolores Hambardzumyan
Department of Neurosurgery, Perelman School of Medicine, University of Pennsylvania, Philadelphia, PA, USA
E-mail: hambardd@PennMedicine.upenn.edu

Abstract

Mutations in DNA mismatch repair (MMR) pathway genes (*MSH2*, *MSH6*, *MLH1*, and *PMS2*) are linked to acquired resistance to temozolomide (TMZ) and high tumor mutation burden (TMB) in high-grade gliomas (HGG), including glioblastoma (GBM). However, the specific roles of individual MMR genes in the initiation, progression, TMB, microsatellite instability (MSI), and resistance to TMZ in glioma remain unclear. Here, we developed *de novo* mouse models of germline and somatic MMR-deficient (MMRd) HGG. Surprisingly, loss of *Msh2* or *Msh6* does not lead to high TMB, MSI, nor confer response to anti-PD-1 in GBM. Similarly, human GBM shows discordance between MMR gene mutations and TMB/MSI.Germline MMRd leads to promoted progression from low-grade to HGG and reduced survival compared to MMR-proficient (MMRp) tumor-bearing mice. This effect is not tumor cell intrinsic but is associated with MMRd in the tumor immune microenvironment, driving immunosuppressive myeloid programs, reduced lymphoid infiltration, and CD8+ T cell exhaustion. Both MMR-reduced (MMRr) and MMRd GBM are resistant to temozolomide (TMZ), unlike MMRp tumors. Our study shows that KL-50, a imidazotetrazine-based DNA targeting agent inducing MMR-independent cross-link–mediated cytotoxicity, was effective against germline and somatic MMRr/MMRd GBM, offering a potential therapy for TMZ-resistant HGG with MMR alterations.

Introduction

The current standard of care for GBM comprises maximal safe surgical resection followed by radiation therapy (RT) and concurrent and adjuvant administration of the alkylating agent temozolomide. Despite this multimodal therapeutic regimen, outcomes remain dismal, with a median overall survival of 13 - 24 months (1), and a 5-year relative survival rate of ~6.8% (2). The clinical benefit of TMZ for primary GBM is modest and is restricted to patients whose tumors harbor promoter methylation-mediated silencing of the enzyme *O*^{6}-methylguanine-DNA methyltransferase (MGMT), which serves as a predictive biomarker of an initial positive response to TMZ (3). However, patients ultimately recur and develop TMZ resistance (4), leaving few treatment options.

TMZ efficacy depends on an intact DNA mismatch repair (MMR) pathway, composed of *MSH2*, *MSH6*, *MLH1*, and *PMS2*. In the absence of MGMT, O6-methylguanine (O6-meG) mispairs with thymine (T), and MMR repeatedly excises thymine in futile cycles that generate single-strand gaps that evolve to double-strand breaks, leading to cell death (5-8). In response to TMZ treatment, GBM may acquire subclonal mutations in MMR genes, which prevents recognition of *O*^{6}-meG: T and preventing tumor cell death. Surviving tumor cells accumulate a massive number of DNA mismatches, resulting in a characteristic cytidine-to-thymidine “hypermutator (HM)” phenotype (4, 9).

Monoallelic germline variants in MMR genes result in Lynch syndrome, which predisposes individuals, particularly those with *MSH2* mutations, to various cancers, including brain cancer (10-12). Biallelic germline mutations in MMR genes cause constitutional mismatch repair deficiency (CMMRD), a pediatric cancer predisposition syndrome characterized by early-onset HM tumors, nearly 40% of which are high-grade gliomas (pHGG) (13). Despite their resistance to alkylating agents, the biology and therapeutic vulnerabilities of MMRd gliomas remain poorly understood, partially due to the lack of mouse models for Lynch syndrome and CMMRD that develop gliomas rather than extracranial tumors (14, 15).

In sporadic post-TMZ HGG, MMR mutations are subclonal (4), whereas in CMMRD pHGG, they are clonal. Both tumor types display HM and resistance to TMZ; however, only the latter responds durably to immune checkpoint blockade (ICI) (16). Since mutations in MMR pathway genes are rare in primary GBM, their role in causing HM in tumor cells of glial origin remains largely understudied. Moreover, since MMR mutations and HM co-occur after TMZ treatment, it is difficult to know whether a single MMR gene mutation can cause HM, or if they are necessary but not sufficient for creating HM (17).

Here, we elucidated the role of MMR genes *MSH2* and *MSH6* in the initiation and progression of GBM, HM formation, and responses to TMZ and ICI using genetically engineered mouse models (GEMMs) of *de novo* gliomas. We show that germline, but not somatic, loss of *Msh2* accelerates GBM progression, remodels the tumor immune microenvironment (TME), towards more immunosuppressive myeloid cells, reduces lymphoid infiltration, and increases exhaustion of CD8+ T cells, and confers resistance to TMZ. Like most of their human counterparts, *Msh2*-deficient GBM do not show increased tumor-mutational burden (TMB) or microsatellite instability (MSI). Like human sporadic post-TMZ GBM, these tumors are resistant to anti-PD-1 treatment, suggesting that subclonal HM and MMR mutations are probably not the cause of ICI failure in GBM. *Msh2*-deficient GBM remain sensitive to KL-50, a imidazotetrazine that induces DNA interstrand cross-links independently of MMR (18-20), revealing therapeutic avenues for patients with Lynch syndrome, CMMRD, and recurrent GBM.

Results

Discordance between MMR gene mutations and HM Phenotype in human GBM

To characterize the behavior of MMR gene alterations in GBM (*MSH2, MSH6, MLH1,* and *PMS2*), and to evaluate their association with HM phenotype and MSI, we analyzed genomic data from AACR project the GENIE v17.0 dataset (21). The dataset was refined to include only adult isocitrate dehydrogenase (IDH) wild-type (WT) primary GBMs using the provided metadata. This process yielded a final study cohort of 3,742 patients, hereafter referred to as the GENIE-GBM cohort. To investigate the putative driver genes in GBM, we used an analysis based on the nonsynonymous rate/synonymous rate (dN/dS) to identify genes evolving under positive selection. Among the top 100 frequently mutated genes in the GENIE-GBM cohort, 42 genes exhibited a significant signal of positive selection. Notably, *MSH2* was included, suggesting its putative driver function in GBM (Figure 1A). In contrast, *MSH6*, a known contributor to TMZ resistance and HM phenotypes in GBM (4), did not show evidence of positive selection in our analysis (Figure 1A).

While we did not integrate the functional mutation type in the dN/dS analysis, we observed a clear trend across the positively selected genes. These genes segregated into two subsets based on the predominant mutation type observed; some were preferentially altered by missense mutations, while others were enriched for truncating mutations (Figure 1A). This pattern reflects the known functional dichotomy between oncogenes and tumor suppressor gene. Oncogenes typically promote tumorigenesis when activated, often through gain-of-function missense mutations. In contrast, tumor suppressor genes inhibit cancer progression and are typically inactivated by truncating mutations.

We hypothesized that the distribution of mutation types could be used to infer the functional class of each gene. To test this, we examined the mutation spectra (nonsynonymous, truncating, and predicted pathogenic mutations) of the top 100 frequently altered genes (Figure 1B). Genes clustered according to their putative function: tumor suppressors such as *NF1*, *RB1*, and *PTEN* were clearly distinct from oncogenes like *EGFR* and *PDGFRA*. MMR genes, including *MSH2*, exhibited mutation profiles more similar to tumor suppressors. Specifically, *MSH2* showed a higher proportion of truncating mutations compared to *MSH6*, suggesting that its loss-of-function may contribute to oncogenesis (Figure 1C, Supplemental Figure 1A).

Given the established correlation between MMR gene defects and HM phenotype, particularly for *MSH6* in the context of GBM, we examined the relationship between MMR gene mutations and TMB (Figure 1D, Supplemental Figure 1B). All MMR genes showed significant association with TMB when mutated (adjusted p-value < 0.001 for *MSH2*, *MSH6*, *PMS2* genes and 0.002 for MLH1 gene); however, the extent of TMB increase differed by mutation type. Interestingly, for *MSH2*, the most frequently altered MMR gene in the GENIE-GBM cohort, missense mutations predicted to be benign (based on AlphaMissense score) (22) did not correlate with increased TMB, whereas the corresponding benign-predicted missense mutations in *MSH6* and *PMS2* did. These results suggest that the pathogenic mutations, and not merely the presence of an *MSH2* mutation, are critical for HM phenotype.

Based upon these findings, we restricted our downstream analysis to pathogenic mutations (including pathogenic missense, truncating, and splice-site mutations). Not all GBMs harboring pathogenic MMR mutations exhibited the HM phenotype, and the incidence of HM varied across different MMR genes (Figure 1E). We next assessed the association between pathogenic MMR mutations and the HM phenotype (Supplemental Figure 1C). All genes except *PMS2* showed a significant association. To identify the most influential MMR gene contributing to HM, we performed multivariate logistic regression analysis (Supplemental Figure 1D). *MSH2* had the strongest association with the HM phenotype, followed by MSH6.

We next used 284 primary IDH WT GBM patients from The Cancer Genome Atlas (TCGA) dataset to investigate the association between tumor mutation TMB and mutations in MMR genes (Supplemental Figure 1E). Six patients harbored nonsynonymous mutations in MMR genes or in *POLE/POLD1*. Among these, *MSH6* mutations were the most frequent (5/284); however, none of the tumors with *MSH6* mutations exhibited HM phenotype. Only two cases demonstrated HM phenotype (0.7%, 2/284). One was an ultra-HM GBM harboring pathogenic missense mutations in both *MLH1* and *POLE*, while the other HM case carried no mutations in any of the MMR genes. No correlation was observed between TMB and MSI status. All tumors were microsatellite-stable except for one case classified as MSI-low (MSI score = 6.96). Overall, these data suggest that *MSH2* may have a potential oncogenic role in GBM. Our analysis further shows that only a subset of GBM samples with MMR gene mutations displayed increased TMB and MSI. Notably, the magnitude of this effect varied depending upon the specific MMR gene involved, with the highest levels of TMB observed in tumors harboring *MSH2* mutations.

Germline loss of *Msh2* drives glioma progression from low to high, and the absence of either *Msh2* or *Msh6* significantly shortens the survival time of mice with HGG

To investigate the biological relevance of correlative human data implicating *MSH2* as a potential oncogenic factor in GBM, we generated a series of GEMM of gliomas harboring either germline or somatic MMR gene loss. To develop mouse models of gliomas with germline MMRd or MMR-reduced (MMRr), we combined the replication-competent avian sarcoma-leukosis virus long terminal repeat with a splice acceptor/tumor virus A (RCAS/Tv-a) system for *de novo* brain tumor generation (23) with germline *Msh2* (14) and *Msh6*-deficient (15) mice (mice with null mutations will be referred to as *Msh2*$^{-/-}$ and *Msh6*$^{-/-}$). We used *Nestin-tva* (*Ntv-a*) transgenic animals to obtain the following crosses: *Ntv-a; Msh2*$^{+/+}$, *Ntv-a; Msh2*$^{+/-}$, *Ntv-a; Msh2*$^{-/-}$, *Ntv-a; Msh6*$^{+/+}$, *Ntv-a; Msh6*$^{+/-}$ and *Ntv-a; Msh6*$^{-/-}$ mice. Tumors were generated by overexpression of PDGFB using RCAS-PDGFB in *nestin*-positive stem/progenitor cells in mice at postnatal days 0-3 (23) (Figure 2A). Kaplan-Meier survival curves demonstrate that homozygous loss of *Msh2,* but not *Msh6,* results in increased tumor incidence and shortened survival of tumor-bearing mice (Figure 2B). WT mice develop gliomas with various histological grades, which are equivalent to grade 2 (lacked brisk mitotic activity (< 3 mitotic figures in the entire section examined) and lacking nuclear atypia, such as pleomorphism, nuclear hyperchromasia, and prominent nucleoli), grade 3 (3 or more mitotic figures detected within the examined tumor sections, but lacking evidence of microvascular proliferation and palisading tumor necrosis), early grade 4 (microvascular proliferation without pseudopalisading necrosis), and grade 4 (microvascular proliferation with pseudopalisading necrosis) IDH WT GBM in humans (24) (Figure 2, C and D). Homozygous loss of *Msh2* (MMRd) resulted in the development of early grade 4 and grade 4 GBM in mice. These results suggest that loss of *Msh2* leads to low grade-to-high grade transition of gliomas. Next, we used the overexpression of the less potent oncogenic driver PDGFA. Since overexpression of PDGFA alone is insufficient to generate tumors, it was combined with *Tp53* silencing using RCAS-shRNA-p53. Loss of *Msh2* results in shortened survival of tumor-bearing mice (Figure 2E) and increased incidence of early grade 4 and grade 4 HGG (Figure 2E), suggesting the effect of *MSH2* on low-to-high transition in gliomas is oncogene-independent. To determine whether dose-dependent loss of *Msh2* or *Msh6* results in increased growth in HGG-bearing mice, we next generated tumors with RCAS-PDGFB and RCAS-shRNA-p53 in *WT*, *Msh2*-reduced (heterozygous loss), *Msh6*-reduced, or deficient mice. Our results indicate that homozygous loss of *Msh2* results in shortened survival of tumor-bearing mice (Figure 2F), while both decrease or loss of *Msh6* results in shortened survival time of tumor-bearing mice (Figure 2G). In human cells, mismatch recognition is attributed to two heterodimeric complexes – MSH2-MSH3 and MSH2-MSH6. Both of those complexes interact with MLH1-PMS2 and are critical for maintaining genomic stability (25, 26). Therefore, *MSH2* is a central MMR gene, because the loss of *MSH2* inactivates the activity of both mismatch recognition heterodimers, so it is expected that *MSH2* deficiency causes strong cancer predisposition in both mice and humans (26). Together with our results showing greater impact of *Msh2* loss compared to *Msh6* loss during the low-to-high transition and despite the significant effect of losing both on HGG growth, we focused on tumors that are deficient in *Msh2*. Immunohistochemistry (IHC) staining for MSH2 and MSH6 in tumors generated in *Ntv-a; Msh2*$^{+/+}$, *Ntv-a; Msh2*$^{+/-}$, and *Ntv-a; Msh2*$^{-/-}$ mice show the absence of MSH2 staining in *KO* mice and reduced MSH6 compared to *WT* control tumors (Supplemental Figure 2A).

To investigate the degree of changes in tumors due to *Msh2* loss, we performed a series of IHC staining, which showed no changes in OLIG2 and GFAP expression levels (Supplemental Figure 2B). However, there was an increase in tumor proliferation from *Msh2*-deficient mice, as assessed by pH3 staining (Supplemental Figure 2B), in accordance with Kaplan-Meier survival results (Figure 2C). Additionally, no changes in vessel area or size (CD31^{+} cells) were observed; however, there was an increase in IBA1-positive tumor area (IBA1 is a pan macrophage marker) (Supplemental Figure 2C). These results indicate that loss of *Msh2* promotes increased cell proliferation and enhances the numbers of tumor-associated macrophages (TAMs) in tumors. This is accompanied by shorter survival of tumor-bearing mice. These results establish *Msh2* as a key driver of low-grade to high-grade glioma progression. Additionally, *Msh2* loss promotes increased progression of HGG through enhanced tumor proliferation and TAM recruitment.

Germline loss of *Msh2*, but not *Msh6*, reduces survival of adult GBM-bearing mice

To compare the role of germline loss of MMR genes when targeting early *nestin*-positive cells (postnatal day 0-2) versus adults (6-10 weeks), we induced tumors with RCAS-shRNA-Nf1, RCAS-PDGFA, RCAS-shRNA-p53 (to generate Nf1 mGBM) or RCAS-PDGFB and RCAS-shRNA-p53 (to generate PDGFB mGBM) combinations in adult *Ntv-a; Msh2*$^{+/+}$*, Ntv-a; Msh2*$^{+/-}$*, Ntv-a; Msh2*$^{-/-}$ mice (Figure 3, A-C) and *Ntv-a; Msh6*$^{+/+}$*, Ntv-a; Msh6*$^{+/-}$, *Ntv-a; Msh6*$^{-/-}$ mice (Supplemental Figure 3A). Kaplan-Meier survival analysis revealed that both homozygous (MMRd) and heterozygous loss (MMRr) of *Msh2* significantly shortened the survival of Nf1 and PDGFB mGBM-bearing mice compared to *WT* mice. In contrast, loss of *Msh6* rendered no significant survival effect (Supplemental Figure 3B). These results aligned with the human correlative analyses in Figure 1A, suggesting a potential oncogenic role of *MSH2* but not *MSH6* in human GBM.

We next evaluated MMRp, MMRr, and MMRd (*Msh2*-driven) tumors for MSH2, MSH6, and MGMT expression levels using immunoblots (Supplemental Figure 4A) and immunofluorescence (IF) staining (Supplemental Figure 4B). The results illustrate *Msh2* gene dose-dependent reduction of MSH2 and MSH6 protein levels, and reduced expression of MGMT (Supplemental Figure 4A). To gain insight into the relevance of the *MSH2* dose-dependent effect on *MSH6* levels in humans, we performed Pearson correlation analysis of *MSH2* versus *MSH6* RNA expression in GBM patient samples from TCGA. Our analysis revealed a strong positive correlation between *MSH2* and *MSH6* RNA expression levels in GBM patient samples (Supplemental Figure 4C). To determine if *Msh6* gene dosage affects MSH2 levels, we induced MMRp, MMRr, and MMRd tumors through *Msh6* gene manipulation (Supplemental Figure 3B). We then assessed expression levels of MSH2, MSH6, and MGMT using immunoblots (Supplemental Figure 4D) and IF (Supplemental Figure 4E). These results were similar to those observed with *Msh2*-induced MMRr and MMRd tumors, except no reductions were observed in MGMT levels (Supplemental Figure 4, A and B).

We then assessed whether *Msh2- and Msh6*-driven MMRd tumors show increased TMB and exhibit MSI. Contrary to what has been documented in other murine tumor types (27), MMRd tumors generated by loss of either *Msh2* or *Msh6* exhibited comparable numbers of mutations as determined by whole-exome sequencing (WES) (single nucleotide variant (SNV) counts in coding regions per Mb of DNA) and MSI scores (28) to MMRp tumors (Figure 3D). This raised the question of whether the increased proliferation and shortened survival time of MMRd tumors (compared to MMRp) and/or the rapid onset of these tumors may lead to a more unified clonality of MMRd tumors, as they do not have enough time to accumulate additional mutations. To address this question, we then cultured three primary *Msh2*-driven MMRd and MMRp tumors *in vitro* for up to 9 months and then performed WES (Supplemental Figure 5A). Our results indicate that culturing MMRd and MMRp tumors for 9 months did not cause an increase in TMB or MSI (Supplemental Figure 5, B-E). This contrasts with what was shown with *Msh2* loss in lung cancer cultures from genetic model (27) and murine breast and colon cancer cell lines - 4T1 and CT26, both of which were generated by the deletion of *Msh2* using CRISPR-Cas9 technology and after serial passages of cells (29, 30). Although in human GBM the highest levels of TMB and MSI are observed in tumors harboring *MSH2* mutations, ~ 50% of *MSH2* mutant tumors did not exhibit increased TMB (Figure 1E). It is important to note that some adult sporadic GBM does not show apparent MSI, likely because bulk whole-genome sequencing (WGS) cannot detect it due to high clonal intra-tumoral heterogeneity in the setting of MMRd. However, it can be detected by single-cell WGS (4). These results indicate that loss of either *Msh2* or *Msh6* alone is likely insufficient to induce high TMB in adult glioma cells, and our models may mimic the fraction of human GBM with MMR mutations that do not exhibit increased TMB or MSI. Further studies are needed to assess whether mutation or loss of the *Pole* gene can demonstrate genetic cooperation with *Msh2* or *Msh6* in generating high TMB and MSI in GBM, similar to what was shown in endometrial cancer mouse models (31) or to examine whether the cell-of-origin and/or timing of tumor initiation also plays a role.

To understand what drives the shortened survival in *Msh2* loss-driven MMRd tumor-bearing mice, we conducted IHC to investigate the degree of changes in MMRd and MMRr tumors; we observed no alterations in the expression of OLIG2 or GFAP (Supplemental Figure 6A). However, there were increased changes in vessel area and size (CD31+ cells), suggesting increased angiogenesis (Supplemental Figure 6B) and increases in IBA1-positive TAM occupied areas (Figure 3, E and F).

Single-cell RNA sequencing (scRNA-seq) indicates loss of *Msh2* increases the tumor cell fraction and contributes to an increased immune-suppressive TME

Given the increased angiogenesis and IBA1 positivity observed in MMRd tumors compared to MMRp tumors, the absence of increased TMB and MSI, and the differences in survival rates of tumor-bearing mice, we next examined whether changes in the expression profiles of various cell types in MMRr and MMRd tumors contribute to the shortened survival of tumor-bearing mice. We performed scRNA-seq on 117,156 cells from 11 murine tumors (whole tumor), with 4, 4, and 3 biological replicates from *Msh2*$^{+/+}$, *Msh2*$^{+/-}$, and *Msh2*$^{-/-}$ mice, respectively (Figure 3G, Supplemental Table 4). We performed unsupervised clustering and systematically annotated cell clusters based upon the consistent expression of known cell type markers (Figure 3H, Supplemental Figure 7A). Tumor cells were annotated based upon their expression of *RCAS, Rfp* (red fluorescent protein), *Olig1*, *Olig2*, *Pdgfra,* and *Sox11* (Supplemental Figure 7A). We next confirmed dose-dependent reduction of *Msh2* expression levels in tumors (Supplemental Figure 7B). *Msh2*$^{-/-}$ tumors showed increased proportions of neoplastic cells and reduced presence of cells that constitute TME (Figure 3, I and J), which was correlated with an increased proportion of cycling cells across all tumor cells (Figure 3K), the majority of which were double positive for Ki67 and OLIG2 by multiplex immunofluorescence (IF) staining (Figure 3L). To evaluate heterogeneity amongst neoplastic cells, we next scored our scRNA-seq data for the four human GBM cell states defined in Neftel et al. (32): Oligodendrocyte Precursor Cells (OPC)-like, Neuron Progenitor Cells (NPC)-like, Astrocyte (AC)-like, and Mesenchymal (MES)-like. Our results demonstrate that the four cellular states are also expressed in our murine tumors (Figure 3M), and that a dose-dependent reduction in *Msh2* has no impact on the prevalence of certain states (OPC/NPC and AC/MES) (Figure 3N).

We next proceeded with the evaluation of TME constituents in our scRNA seq dataset. Infiltrating myeloid cells and brain resident microglia represented the largest components of the TME and accounted for ~ 46% of all sequenced cells (Figure 4A). Within the myeloid cells, microglia, monocytes, and monocyte-derived macrophages (MDM) together composed most of the cells (Figure 4B). We next proceeded to evaluate these results at the protein level by performing multiplex flow cytometry. We analyzed tumors at the endpoint of survival experiments using spectral flow cytometry (Figure 4C, Supplemental Figure 8). We used marker combinations and gating strategies to distinguish between various myeloid subsets based upon our published protocols (33, 34). There was an increase in infiltrating bone marrow-derived myeloid cells (BMDMs) in MMRr tumors (Figure 4C), further supporting increased IBA1 staining by IHC (Figure 3E). There were reductions in DC1 in MMRd compared to MMRp tumors (Figure 4C, Supplemental Figure 8).

Since we did not observe major changes in myeloid composition in MMRr or MMRd tumors, we next evaluated if the phenotypes of the major myeloid cell types are affected. To investigate microglial diversity, we categorized microglia into four major clusters (Figure 4D) based upon the expression of key cluster genes (34) (Supplemental Figure 7C). Interestingly, disease-associated microglia (DAM) showed an increased fraction in both MMRr and MMRd tumors (Figure 4D). DAM is known for increased expression of immunosuppressive molecules, including *Lgals3* and *Hmox1,* and decreased expression of antigen presentation machinery and pro-inflammatory genes (34). Similarly, when we clustered monocytes and MDMs into phenotypic clusters, we observed increased expression of disease-associated monocyte and MDM clusters in MMRr tumors (Figure 4, E and F, Supplemental Figure 7, D and E). We have previously documented that decreasing DAM clusters was associated with better survival in H3K27M mutant diffuse midline gliomas (DMG) (34). In human GBM, increased expression of the immune checkpoint PD-L1/PD-1 axis is associated with inferior survival (35). We have previously documented that PD-L1 is mainly expressed by myeloid cells in murine GBM (36). Next, we evaluated the expression levels of *Cd274* (gene coding PD-L1 protein) in our scRNA-seq data (Figure 4G) and mean fluorescent intensity (MIF) of PD-L1 protein expression by flow cytometry (Figure 4H) in myeloid subsets in MMRp, MMRr, and MMRd tumors. Our results demonstrate increased PD-L1 expression in various myeloid fractions, especially in microglia in MMRd tumors (Figure 4H). Overall, we observed higher relative expression of immunosuppressive pathways in various myeloid subsets in MMRr and MMRd tumors compared to MMRp tumors. scRNA-seq data show that all tumors irrespective of *Msh2* gene status exhibit reduced *Cd80* expression, but MMRp tumors show higher expression of *Cd86* in all myeloid subsets - most notably in microglia. In contrast, *Cd80* expression is reduced in MMRr and MMRd tumors (Supplemental Figure 9A). These results suggest that *Msh2*-altered tumors exhibit broader suppression of co-stimulatory signaling in the tumor myeloid compartment. MHCII molecules - *H2-Aa*, *H2-Ab1* and *H2-Eb1* are highly expressed in WT monocytes and MDMs, less in microglia, and are decreased in *Msh2*-reduced tumors, suggesting reduced antigen presentation. FACS results confirmed scRNA-seq data showing higher expression of MHCII in monocytes and MDM compared to microglia in WT tumors (Supplemental Figure 9B), which does not change based upon *Msh2* gene mutation status, although trends towards reduction were apparent in *Msh2*-reduced tumors (Supplemental Figure 9C). IHC analysis demonstrated that areas of activated CD68+ TAMs, CD206+ immunosuppressive TAMs, and microglia within both the tumor core and invasive edge were not altered by *Msh2* gene status (Supplemental Figure 10).

To functionally characterize spatial relationships between TAMs with CD8+ and CD4+ T cells in MMRp vs. MMRd tumors we used Orion multiplex IF platform, which is a panel of 14 antibodies specific for various cell types on 4 MMRp and 4 MMRd tumors (Supplemental Figure 11, A-G). We quantified the distance of TAMs (IBA1+/F480+ double positive) from PD-1+CD4+ T and PD-1+CD8+ T cells and found close co-localization to TAMs irrespective of MMR status (Supplemental Figure 11H). To further characterize TAMs, we double stained them with CD163 and evaluated their abundance in tumor area and in perivascular areas (marked as 30μm EC area) (Supplemental Figure 11I). Due to a limited number of antibodies that can be used in spatial multiplex IF along with the low abundance of T cells - especially those co-expressing PD-1 - in 5 μm tumor sections constrained detailed lymphoid phenotyping. To address this, we used scRNA-seq and flow cytometry on whole tumors to determine how myeloid-driven immunosuppression influences the lymphoid compartment in MMRp, MMRr and MMRd tumors. In MMRr and MMRd tumors, we observed a lower relative abundance of total lymphoid fraction (Figure 5A), including NK, T cells, plasma, and B cells compared to MMRp tumors (Figure 5B, Supplemental Figure 12A). We then separated B and plasma cells and further delineated T-cell subsets based upon lineage and functional markers (Supplemental Figure 12A, Figure 5, C and D). We observed relatively lower abundance of naïve CD8+ T cells and proliferating T cells in MMRr and MMRd (Supplemental Figure12 A).

Next, we used multicolor flow cytometry with a larger cohort to determine whether our scRNA seq observations are similarly valid at the protein level (Figure 5E, Supplemental Figure 12B). We used marker combinations and gating strategies to distinguish between various lymphoid subsets based upon our published protocols (33, 34). Flow cytometry data, in conjunction with scRNA-seq analysis, revealed decreases in total lymphoid cells, B cells, NK cells, and T cells in MMRd tumors compared to MMRp tumors. These effects were not observed in MMRr tumors (Figure 5E, Supplemental Figure 12B). Since we observed a higher relative abundance of disease-associated clusters in various myeloid subsets and elevated expression of PD-L1 is associated with increased exhaustion of T cells, we evaluated the expression of various genes encoding immune checkpoint molecules on CD4+ and CD8+ T cells, including cytotoxic T lymphocyte antigen-4 (CTLA-4 – *Ctla4*), T cell immunoglobulin and mucin protein-3 (TIM-3 – *Havcr2*), lymphocyte activation gene-3 (LAG-3 – *Lag3*) and programmed cell death protein-1 (PD-1 – *Pdcd1*) in MMRp, MMRr and MMRd tumors. We observed higher relative expression of all immune checkpoints in CD8+ T cells in MMRd tumors relative to MMRr and MMRp (Figure 5F), which we further confirmed by flow cytometry for PD-1 and TIM3 (Figure 5G). PD-L1 expression is low in myeloid cells of MMRp tumors (Figure 4G), similar to what was shown in human GBM (35) and in contrast to brain metastasis (37), which has been suggested as a contributor to the lack of association seen between PD-L1 expression in tumors and survival in clinical trials evaluating ICI for GBM (38). To functionally characterize CD8+ T cells, we conducted T cell–tumor cell co-culture experiments to first evaluate the impact of *Msh2* heterozygosity on stimulated CD8+ T-cell proliferation and effector cytokine production, and then to assess the effects of co-culturing MMRp and MMRd primary GBM stem-like cells (GSCs) on these functions (Supplemental Figure 13A). Our results indicate that while proliferation is not affected, effector cytokine production is reduced in stimulated CD8+ T cells from *Msh2* heterozygous mice, suggesting reduced activation or increased exhaustion. Further, co-culture of stimulated *WT* and *Msh2* heterozygous CD8+ T cells with *MMRp* and *MMRd* GSCs markedly reduced production of effector cytokines, including Granzyme

B and IFNγ, and only MMRd GSCs were able to diminish TNFα levels. These findings indicate that CD8+ T-cell proliferation is unaffected by *Msh2* reduction, but effector cytokine production is reduced, which is further reduced by co-culture with tumor cells, particularly MMRd GSCs (Supplemental Figure 13B). These results show that heterozygous loss of *Msh2* dampens CD8+ T-cell effector function without affecting proliferation and is exacerbated by co-culture with MMRd GSCs.

In MMRd tumors, we observed increased expression of both PD-L1 and PD-1; we therefore asked whether these tumors will respond to anti-PD-1 therapy. We performed an experiment to evaluate the effects of anti-PD-1 antibodies in MMRp, MMRr, and MMRd tumor-bearing mice. We started treatment at an earlier tumor development stage and continued until the mice reached the humane endpoint, as illustrated in Figure 5H. Kaplan-Meier survival curves illustrate no differences in survival of MMRp, MMRr, and MMRd tumor-bearing mice treated with isotype control or anti-PD-1 antibodies (Figure 5H). Our results indicate that MMRd tumors contain a lower percentage of lymphoid cells and show an increased number of tumor cells with higher proliferation rates, raising questions about how much each of these factors contributes to shortened survival. To determine whether lymphoid fraction reduction contributes to the shortened survival of MMRd tumors induced by *Msh2* loss, we evaluated lymphoid recruitment in both MMRr and MMRd tumors induced by *Msh6* loss, which did not result in survival differences compared to *Msh6 WT* GBM-bearing mice. Our findings show that the survival of tumor-bearing mice is not affected by either MMRr or MMRd induced by *Msh6* (Supplemental Figure 3). Flow cytometry of lymphoid subsets showed no changes in lymphoid, NK, B cells, or T cells in *Msh6*-induced MMRd tumors and in contrast to *Msh2*-induced MMRd tumors (Supplemental Figure 12C). Overall, these results suggest that reduced lymphoid recruitment in *Msh2*-deficient tumors may contribute to tumor aggressiveness.

Somatic MMRd does not confer shortened survival in GBM

To investigate the role of tumor cells in the aggressiveness of MMRd tumors in the context of germline mutation (in all cells), we developed somatic MMR-deficient models (MMRd only in tumor cells). We adopted our autochthonous *Ntv-a* mouse model of GBM by breeding into conditional *Msh2* (39) and *p53* (40) knockout alleles (*Ntv-a; $Msh2^{fl/fl}$; $p53^{fl/fl}$* and *Ntv-a; $Msh2^{fl/WT}$; $p53^{fl/fl}$* mice). Intracranial delivery of RCAS-PDGFB and RCAS-Cre successfully created *Msh2* (reduction or loss) and *Tp53* loss only in tumor cells (Figure 6A). Kaplan-Meier survival analysis shows that the presence of somatic MMRr or MMRd did not affect the survival of tumor-bearing mice compared to WT controls (Figure 6B**)**, in contrast to germline MMRr or MMRd tumor-bearing mice with shortened survival (Figure 3, B and C). Furthermore, there were no differences in tumor grade distribution between MMRp and somatic MMRr or MMRd tumors (Supplemental Figure 14A). Combined loss of *Msh2* and *p53* without PDGFB was not sufficient to induce tumors (Supplemental Figure 12D). To complement our findings, we created a somatic MMRd model where *Pten* was co-deleted with *Msh2* by generating a *Ntv-a; $Msh2^{fl/fl}$; $Pten^{fl/fl}$* cross. Intracranial delivery of RCAS-PDGFB and RCAS-Cre successfully created tumors with *Msh2* (reduction or loss) and *Pten* deficiency only in tumor cells. Kaplan-Meier survival analysis shows that the presence of somatic MMRr or MMRd did not affect the survival of tumor-bearing mice compared to WT controls (Figure 6C). IHC staining of tumors from somatic MMRr and MMRd showed a dose-dependent decrease in *MSH2* levels in tumor cells (Figure 6D). However, no changes were detected in the proportion of different cell types (TAMs, microglia, and neutrophils) or vessels area and size (CD31+ cells) within the tumor microenvironment (Supplemental Figure 14B) among these genotypes. In addition, no differences in proliferation were observed between MMRp and MMRd tumors, as assessed by pH3 staining (Supplemental Figure 14B), consistent with the Kaplan-Meier survival results (Figure 6B). We created primary GSC cultures from MMRp and MMRd tumors and assessed their growth using the MTS colorimetric cell growth assay (Figure

6E). Similar to the *in vivo* survival curves (Figure 6B), the results showed no differences in the growth of MMRp and MMRd primary tumor cultures (Figure 6F). We next generated a series of crosses to allow us to specifically delete *Msh2* in CX3CR1-positive myeloid cells (monocytes, MDM, and microglia), CD4+ T and CD8+ T cells (Illustration in Figure 6G**).** Kaplan-Meier survival curves indicated no differences in survival, although a trend was observed in *Msh2*-deficient CD8+ T cell only mice (Figure 6H). These results suggest that the reduced survival in mice with germline MMR deficiency is due to combined effects of altered tumor immune microenvironment and tumors cells caused by *Msh2* loss.

MMRr and MMRd GBM-bearing mice confer resistance to TMZ in GBM-bearing mice

Silencing MGMT has been shown to serve as a predictive biomarker of response to TMZ in GBM (3). When the MGMT promoter is methylated, it results in RNA expression silencing, correlating with reduced or absent protein levels (41), leading to enhanced anti-tumor toxicity by TMZ. Our tumors exhibit varying levels of MGMT expression (Supplemental Figure 4, A and D). To assess *Mgmt* expression levels, we performed qRT-PCR in naïve brains, tumor samples (tumor + TME), and freshly-sorted RFP-positive tumor cells. Our results showed no differences in *Mgmt* expression levels in naïve and tumor brains, but reduced expression in freshly-sorted tumor cells (Supplemental Figure 15A). We next conducted immunoblots to assess MGMT protein levels in presorted (single cell suspensions from fresh tumors), RFP+ (sorted tumor cells), and RFP-negative cells (TME cells), revealing variable expression of MGMT, but with higher expression in pre-sorted and RFP- cells compared to RFP+ tumor cells. We then sorted tumor cells into RFP-high and RFP-low groups and conducted an immunoblot for MGMT. We observed that MGMT expression does not correlate with RFP intensity and is lower than in pre-sorted cells (Supplemental Figure 15B). This indicates that GBM contains various proportions of tumor cells expressing various levels of MGMT. This is also evident from immunoblots of fresh tumors showing various degrees of MGMT expression (Supplemental Figure 4, A and D). Cultured primary cells from these tumors showed no MGMT expression (Supplemental Figure 15C). This could be because culture conditions are selecting survival of MGMT low/not-expressing cells or MGMT expression is being silenced in cultures. Meanwhile, MSH2 and MSH6 expression levels were not affected by culture conditions (Supplemental Figure 15C**)**. To check if the loss of MGMT expression in our primary tumor cell cultures is unique, we conducted immunoblots for MGMT in various established murine cancer cell lines, all of which displayed no MGMT expression (Supplemental Figure 15D). Based upon our results, we hypothesized that tumors *in vivo* contain a mix of tumor cells with high and low expression of MGMT. This suggests that treatment with TMZ will demonstrate anti-tumor efficacy by targeting MGMT-low/silenced cells, establishing our models as valuable tools for studying TMZ resistance driven by MMRd.

To determine if MMRr tumors behave similarly to MMRd, we created germline MMRp, MMRr, and MMRd PDGFB mGBM. Based on the median survival time of each group, we then treated tumor-bearing mice with two cycles of clinically relevant doses of TMZ after 25 days (for MMRr and MMRd tumors) and 30 days (for MMRp tumors) post-injection (Figure 7A**)**. Our results indicate an increase in the survival of MMRp tumor-bearing mice compared to the VEH group, but not for MMRr and MMRd mice (Figure 7B). In the VEH group, we observed a reduction in total lymphoid cells, CD8+ T cells, B cells, and NK cells at 7 days post-treatment. This reduction is likely due to increased tumor burden in mice and reaching the survival endpoint, as we have previously demonstrated (42). When we analyzed the immune cell populations from the blood of MMRp tumor-bearing mice at day 7 post-treatment, we found that TMZ treatment resulted in a reduction of CD4+ T cells, total myeloid cells, and monocytes compared to pre-treatment (Figure 7D, upper panel). However, these differences were not observed in the blood before or after TMZ treatment in either *Msh2* or *Msh6*-induced MMRr and MMRd tumor-bearing mice (Figure 7D, lower panel). The reductions in these cell populations that have been shown to exhibit pro-tumorigenic function could be contributing to the survival benefit seen in MMRp tumor-bearing mice with TMZ treatment. When we compared the TME of MMRp tumors at the survival endpoint, we observed a decrease in total BMDMs, MDMs, Tregs, DC1, and DC2 in the TMZ group compared to the VEH group. No differences were observed in MMRr and MMRd tumors treated with TMZ (Figure 7E). Overall, these results demonstrate that TMZ treatment shows anti-tumor efficacy in MMRp tumor-bearing mice, but not in *Msh2*- and *Msh6*-driven MMRr and MMRd-tumor-bearing mice.

KL-50 treatment improves the survival in somatic and germline MMRd tumor-bearing mice

Our results indicate that MMRp tumors contain cells with varying levels of MGMT expression. Treatment with TMZ extends the survival of MMRp tumor-bearing mice in contrast to MMRr and MMRd tumor-bearing mice. Next, we aimed to assess the effectiveness of KL-50 treatment and fully characterize the response of MMRp, MMRr, and MMRd tumors, as well as its impact on the immune TME and blood profiles of tumor-bearing mice. KL-50 is a imidazotetrazine-based agent that induces DNA interstrand crosslinks (ICLs) and subsequent double-stranded breaks in an MMR pathway-independent manner. KL-50 is designed to transfer a 2-fluoroethyl substituent to O^6-G, thereby generating O^6-(2-fluoroethyl) guanine (O^6-FEtG) that can be directly repaired by MGMT. In the absence of MGMT, O^6-FEtG undergoes hydrolytic rearrangement, resulting in the formation of G–C interstrand crosslinks and cytotoxicity that does not rely on "futile cycling" through the MMR pathway (18, 19, 43). While this mechanism is similar to lomustine, which is commonly used in TMZ-resistant GBM, the kinetics of ICL formation are slower with KL-50, allowing MGMT-proficient healthy cells to reverse DNA alkylation (43). We created somatic MMRp and MMRd by injecting PDGFB + Cre in *Ntv-a; Msh2* $^{wt/wt}$; *p53* $^{fl/fl}$ and *Ntv-a; Msh2* $^{fl/fl}$; *p53* $^{fl/fl}$ mice. Nineteen days after the injections, we began KL-50 and VEH treatment, following the schematic illustration in Figure 8A. KL-50 treatment prolonged the survival of both MMRp and MMRd tumor-bearing mice compared to the VEH groups (Figure 8B). We then proceeded to test the effectiveness of KL-50 in tumor-bearing mice with MMRp and germline MMRr tumor-bearing mice. Twenty-five days post injection, we initiated a cycle of KL-50, following the schematic illustration in Figure 8A. KL-50 treatment extended the survival of MMRp and germline MMRr tumor-bearing mice compared to the VEH group (Figure 8C).

To better understand and compare the effects of KL-50 to TMZ (Figure 7), we treated germline MMRp and MMRr tumor-bearing mice with KL-50 or VEH as shown in Figure 8D. We saw a transient reduction of various immune subsets in the blood of VEH-treated mice at 12 days post-treatment. There were no changes observed in the blood of MMRr tumor-bearing mice treated with VEH (Figure 8D). In contrast to VEH-treated animals, the blood of KL-50-treated MMRp tumor-bearing mice at day 12 post-treatment showed severe reductions in nearly all immune cell types assessed. There were reductions in myeloid cells, B cells, NK, and total myeloid cells with no changes in CD4+ and CD8+ T cells (Figure 8F). At 12 days post-treatment, analysis of MMRp tumors revealed increases in microglia, CD8+ T cells, and NK cells. On the other hand, MMRr tumors showed decreases in BMDM and MDM, along with increases in CD8+ T and NK cells (Figure 8E). To assess the immediate impact of KL-50 on tumors, we conducted an MRI-guided experiment, following the steps illustrated in Figure 8F. We conducted a T2-weighted MRI on mice bearing MMRp and MMRr tumors to ensure that both the treatment and VEH groups enrolled sizable tumors with similar volumes and sexes equally distributed in both groups (Figure 8G). Mice were treated with KL-50 at 25 mg/kg or VEH for five consecutive days and subjected to post-treatment MRI imaging. Our data indicate that KL-50 treatment leads to a reduction in tumor growth in both MMRp and MMRr tumor-bearing mice (Figure 8, H and I). An increase in cell death was observed by TUNEL staining only in MMRr tumors (Supplemental Figure 16). The combined effects of reducing immunosuppressive myeloid subsets and increasing CD8+ T and NK cell populations in tumors could also be contributing to KL-50 efficacy. These results demonstrate the anti-tumor efficacy of KL-50 in MMRp and somatic and germline MMRr and MMRd tumor-bearing mice, in contrast to TMZ, which only shows anti-tumor efficacy in MMRp tumors.

Discussion

MMR gene mutations are rare in primary GBM. However, their frequency increases due to TMZ treatment in recurrent GBM and co-occurs with increased TMB (4). This raises the challenge of determining whether MMR mutations drive TMB formation *de novo* or result from TMZ exposure. Prior GBM studies have modeled MMR loss via inducing MSH6 loss through prolonged TMZ exposure (which co-occurs with HM) (44), CRISPR-mediated deletions of *MSH6* (45), or shRNA silencing of *MSH2* (19). These studies focused on evaluating resistance mechanisms to TMZ and explore alternative compounds, but they did not establish the causal role of MMR loss in HM.

To address this knowledge gap, we developed GEMMs of MMRd and MMRr HGG using germline or conditional deletion of *Msh2 or Msh6 in* RCAS/Tva-based glioma models, which faithfully mimic HGG initiation and progression in both neonatal and adult mice (23, 36). In pediatric models, loss of *Msh2*, but not *Msh6*, drives the transition from low- to high-grade glioma, whereas loss of either gene further accelerates *de novo* HGG progression. In adult GBM models, accelerated tumor growth and reduced survival are observed only when MMRr and MMRd is driven by *Msh2* loss, indicating that *Msh2* is a more potent oncogenic driver, whereas the effect of *Msh6* is context dependent.

Germline MMRr and MMRd tumors exhibit MSI and TMB levels similar to those of MMRp GBM, suggesting that MMRd alone does not drive HM in this context. This likely results from timing of tumor initiation, cell-of-origin, and the rapid tumor onset driven by oncogenic PDGFB signaling coupled with loss of *Tp53* or *Pten.* In contrast, *Msh2* loss in autochthonous $KRAS^{G12D}$/*Tp53*-deficient murine lung tumors resulted in increased TMB, an effect further enhanced by *in vitro* passaging of tumor cells (27). GBM diverges from this pattern, as primary MMRd GBM cultures maintain stable TMB and MSI, indicating that *Msh2* loss alone is insufficient to induce HM in glioma cells. Analysis of a limited number of GBM patient samples from TCGA analysis indicates that single MMR gene mutations only increase TMB and MSI when concurrent with *POLE* mutations. These observations suggest that *POLE* mutation may cooperate with MMR gene mutations to promote HM phenotype and underscore the need for further investigation.

We show that the shortened survival times of germline *Msh2*-driven MMRr and MMRd tumor-bearing mice are associated with increased angiogenesis and TAM coverage, increased BMDM infiltration, and reduced lymphoid cell recruitment. ScRNA-seq results revealed increased disease-associated myeloid cell subsets, increased expression of PD-L1, which correlated with reduced lymphoid population, and increased expression of immune checkpoint molecules in CD8+ T cells, including PD-1, suggesting increased exhaustion. Yet, treatment with anti-PD-1 therapy did not result in improved survival of MMRd or MMRr tumors, which showed similar resistance as MMRp tumors. It is plausible that the loss of MMR genes leads to an increase in immune exhaustion and expression of immune checkpoint molecules; however, without increases in TMB and MSI, fails to elicit effective ICI response. Clinical data show that ultra-HM MMRd+DPd pHGGs are characterized by increased PD-L1 expression, which is associated with improved overall survival (OS) in response to ICI (16). Survival of mice with somatic MMRd, MMRr and MMRp tumors were comparable *in vivo*, consistent with similar growth rates of MMRd and MMRp tumor cells *in vitro*. These results indicate that the reduced survival of germline MMRd and MMRr is likely caused by a combination of *Msh2* loss in tumor cells and in the TME, especially CD8+ T cells. Supporting this, *Msh2* heterozygous loss dampened CD8+ T cell effector function without affecting proliferation, which was further enhanced by co-culture with MMRd GSCs.

MMRd induced by TMZ in a subset of TMZ-sensitive cells has been documented in gliomas (4), and even a slight reduction in *MSH2* levels can confer TMZ resistance in GBM (46). These findings show that changes in the expression levels of MMR genes, not only mutations, can affect some of their biological functions. Here, we show that MMRr is sufficient to provide resistance to TMZ in TMZ-sensitive tumors, comparable to MMRd. TMZ treatment reduces circulating and intratumoral myeloid cells, including BMDMs and T regs, populations known to promote GBM growth and immune suppression (47). Severe myelosuppression has been documented in a subset of GBM patients treated with TMZ (48), and lower baseline neutrophil counts correlate with improved outcomes in newly diagnosed GBM, independent of steroid use (49). We observed reduced lymphoid populations in MMRp tumor-bearing mice, consistent with TMZ-induced lymphopenia reported as a poor prognostic factor in GBM (50). Collectively, these findings suggest that TMZ may exert dual effects in the TME in MMRp tumors, simultaneously reducing immunosuppressive cells in tumors while impairing peripheral immune response, similar to what has been shown in human GBM (51).

KL-50, N3-(2-fluoroethyl) imidazotetrazine, was developed to retain TMZ efficacy in MGMT-silenced cells while circumventing the reliance on MMR pathway for its anti-tumor efficacy (19). In contrast to TMZ, KL-50 treatment had comparable anti-tumor efficacy in both somatic MMRp and MMRd tumor-bearing mice, including germline MMRr tumor-bearing mice. Unlike TMZ, KL-50 induced a reduction in microglia, in addition to the reduction in NK and CD8+ T cells in tumors. In MMRr tumors, KL-50 treatment reduced intertumoral BMDMs, MDMs, NK, and CD8+ T cells. In both MMRp and MMRr tumor-bearing mice, treatment with KL-50 resulted in increased cell death by IHC and reduced tumor growth as determined by MRI. These results suggest that KL-50 can be an alternative therapy for TMZ, not only for TMZ-induced MMRd tumors, but also for patients with *de novo* pathways with inherited defects in *POLE* and MMR genes. These models can help to investigate further mechanisms of resistance to TMZ in both primary and recurrent tumors, as well as to explore the biological functions of other MMR genes. Importantly, these models can be used to test whether mutations in multiple MMR genes, alone or combined with *Pole/d* mutations, can create models with MSI and high TMB and determine whether this is cell-of-origin- and age-dependent. These models can then be used to determine if there is a causal relationship between hereditary MMRd/POLE loss and the response to immune checkpoint blockade, along with underlying mechanisms driving this relationship.

Methods

Detailed methods can be found in **Supplemental Methods**.

Sex as a biological variable: Our study examined male and female animals, and similar findings are reported for both sexes.

Mice, virus generation and tumor induction: Adult mice of both sexes (equal distribution in various groups) in the 8-16 weeks age range and newborn mice at the ages of P0-P3 were used for experiments and tumors were generated according to published protocols (23, 42). Specific details regarding various mice used can be found in the Supplemental Methods.

Spectral flow cytometry and flow sorting: Single cell suspensions from were generated as previously described. Cells were stained with primary antibodies (Supplemental Table 1). All data were collected on Cytek Aurora spectral flow cytometer. Data were analyzed using FlowJo, version 10, software (BD Bioscience) based on our published protocols (42).

*In vivo survival experiments with aPD-1, temozolomide, and KL-50 treatments: a*PD-1 (10 mg/kg body weight, Bio X Cell, BE0146) or isotype control antibody aIgG2a (10 mg/kg body weight, Bio X Cell, BE0089) administered intraperitoneally every three days until humane endpoint. TMZ (25 mg/kg body weight, Sigma, T2577) or vehicle control (10μL/g body weight of 0.9% NaCl containing 10% DMSO; McKesson, 2718344) was administered orally using a schedule of five days on, two days off, followed by another five days on (total = 10 doses). KL-50 (25 mg/kg body weight) or vehicle control (10% [2-hydroxypropyl]-β-cyclodextrin; Sigma, 332607) was administered once daily for five consecutive days.

MRI image acquisition: T2-weighted MRI scans of tumor-bearing mice were performed as described (52).

Single-cell RNA sequencing and data analysis: ScRNA-seq using the Chromium 3' V3 platform (10x Genomics) was performed as previously described and data analysis was done following the pipeline of Ross et al. (2024) (34). The sample manifest for scRNA sequencing is provided in Supplemental Table 4.

Immunohistochemistry and Immunofluorescence: All IHC staining was performed on a Bond Rx (Leica Biosystems) and antibodies for IHC and IF are included in Supplemental Table 1 and for multiplex IF in Supplemental Table 2.

RNA extraction and qPCR: RNA extraction and qPCRs were performed based on published protocols and primers are listed in Supplemental Table 3.

GENIE data analysis: We downloaded AACR Project GENIE v17.0 dataset from Synapse (21). Details on analysis are provided in the Supplemental Methods.

Statistics

Graphs were created using GraphPad Prism 8 (GraphPad Software Inc.) or R. Variables from two experimental groups were analyzed using unpaired or paired parametric two-tailed *t*-tests as appropriate, assuming equal standard deviations. A one-way ANOVA was used to compare multiple variables from more than two groups; details for each test are provided in the figure legends. Kaplan–Meier survival analysis was performed using the log-rank Mantel-Cox test and Gehan-Breslow-Wilcoxon test. Data are represented as mean ± SD. Numbers of samples in each group are indicated in the individual figures. Further details are included in the figure legends. $^*P < 0.05$; $^{**} P < 0.01$; $^{***} P < 0.001$; $^{****} P < 0.0001$; ns not significant.

Study approval

All experimental procedures were approved by the Institutional Animal Care and Use Committee of Mount Sinai School of Medicine (Protocol #2019-00619 and #2014-0229) and Perelman School of Medicine, University of Pennsylvania (Protocol #807737).

Data availability

All scRNA-seq raw data are deposited in the Gene Expression Omnibus (GEO) database under accession number GSE292092. Values for all data points shown in the graphs are provided in the Supporting Data Values file. Further information and requests for resources and reagents should be directed and will be fulfilled by the lead contact, Dolores Hambardzumyan (hambardd@PennMedicine.upenn.edu)

Author contributions

The indicated authors were responsible for the following roles. Designing research studies: all authors. Conducting experiments: M.P-V, T.J., K.R., A.B., G.P., G.P., M.D., D.B., R.R., D.H. Analyzing data: M.P-V, T.J., K.R., A.B., G.P., G.P., N.S, S.F., A.A., S-W.C., R.R., E.R., J.C.V., N.M.T., A.T. Providing intellectual input and reagents: R.B., A.B., R.S., J.C.V., A.T., Z.C., S-W.C., R.R., D.H. Writing and editing manuscript: all authors. M.P-V was responsible for creating all the figures with input from N.S, S-W.C and A.T. D.H. wrote the manuscript with input from M.P-V. D.H. conceptualized and supervised the study and obtained funding for it.

Acknowledgements

This work is the result of NIH funding, in whole or in part, and is subject to the NIH Public Access Policy. Through acceptance of this federal funding, the NIH has been given a right to make the work publicly available in PubMed Central.

We thank all members of the Hambardzumyan lab for their valuable input on this study. We appreciate Dr. James Ross and Chris Nelson for their editing contributions. We would like to acknowledge the Flow Cytometry, Pathology, Genomics, and Integrated Cellular Imaging Cores at Mount Sinai for their services. P30 CA196521 supports the Tisch Cancer Institute and related research facilities. This work was supported by NIH/NINDS R01 NS100864, R21 NS1256000, Ian's Friends Foundation, and ISMMS and PSOM seed funding to DH. JCV is supported by the NIH/NCI K08 Career Development award 1-K08 CA258796-01, the Robert Wood Johnson Harold Amos Medical Faculty Development Program, Hyundai Hope on Wheels Scholar Hope Grant, and the Fund to Retain Clinical Scientists at Yale, sponsored by the Doris Duke Charitable Foundation award #2015216. EW is supported by R01CA248536. The authors would like to acknowledge the American Association for Cancer Research and its financial and material support in the development of the AACR Project GENIE registry, as well as members of the consortium for their commitment to data sharing. Interpretations are the responsibility of study authors. Some of the figure illustrations and graphical abstracts were created in BioRender.

References

1. Price M, Ryan K, Shoaf ML, Neff C, Iorgulescu JB, Landi DB, et al. Childhood, adolescent, and adult primary brain and central nervous system tumor statistics for practicing healthcare providers in neuro-oncology, CBTRUS 2015-2019. *Neurooncol Pract.* 2024;11(1):5–25.
2. Ostrom QT, Cioffi G, Gittleman H, Patil N, Waite K, Kruchko C, et al. CBTRUS Statistical Report: Primary Brain and Other Central Nervous System Tumors Diagnosed in the United States in 2012-2016. *Neuro Oncol.* 2019;21(Suppl 5):v1–v100.
3. Hegi ME, Diserens AC, Gorlia T, Hamou MF, de Tribolet N, Weller M, et al. MGMT gene silencing and benefit from temozolomide in glioblastoma. *N Engl J Med.* 2005;352(10):997–1003.
4. Touat M, Li YY, Boynton AN, Spurr LF, Iorgulescu JB, Bohrson CL, et al. Mechanisms and therapeutic implications of hypermutation in gliomas. *Nature.* 2020;580(7804):517–23.
5. Quiros S, Roos WP, and Kaina B. Processing of O6-methylguanine into DNA double-strand breaks requires two rounds of replication whereas apoptosis is also induced in subsequent cell cycles. *Cell Cycle.* 2010;9(1):168–78.
6. Noonan EM, Shah D, Yaffe MB, Lauffenburger DA, and Samson LD. O6-Methylguanine DNA lesions induce an intra-S-phase arrest from which cells exit into apoptosis governed by early and late multi-pathway signaling network activation. *Integr Biol (Camb).* 2012;4(10):1237–55.
7. Silber JR, Bobola MS, Blank A, and Chamberlain MC. O(6)-methylguanine-DNA methyltransferase in glioma therapy: promise and problems. *Biochim Biophys Acta.* 2012;1826(1):71–82.
8. Ganesa S, Sule A, Sundaram RK, and Bindra RS. Mismatch repair proteins play a role in ATR activation upon temozolomide treatment in MGMT-methylated glioblastoma. *Sci Rep.* 2022;12(1):5827.
9. Branch P, Aquilina G, Bignami M, and Karran P. Defective mismatch binding and a mutator phenotype in cells tolerant to DNA damage. *Nature.* 1993;362(6421):652–4.
10. Suwala AK, Stichel D, Schrimpf D, Kloor M, Wefers AK, Reinhardt A, et al. Primary mismatch repair deficient IDH-mutant astrocytoma (PMMRDIA) is a distinct type with a poor prognosis. *Acta Neuropathol.* 2021;141(1):85–100.
11. Aaltonen LA, Peltomaki P, Leach FS, Sistonen P, Pylkkanen L, Mecklin JP, et al. Clues to the pathogenesis of familial colorectal cancer. *Science.* 1993;260(5109):812–6.
12. Therkildsen C, Ladelund S, Rambech E, Persson A, Petersen A, and Nilbert M. Glioblastomas, astrocytomas and oligodendrogliomas linked to Lynch syndrome. *Eur J Neurol.* 2015;22(4):717–24.
13. Wimmer K, Kratz CP, Vasen HF, Caron O, Colas C, Entz-Werle N, et al. Diagnostic criteria for constitutional mismatch repair deficiency syndrome: suggestions of the European consortium 'care for CMMRD' (C4CMMRD). *J Med Genet.* 2014;51(6):355–65.
14. Reitmair AH, Schmits R, Ewel A, Bapat B, Redston M, Mitri A, et al. MSH2 deficient mice are viable and susceptible to lymphoid tumours. *Nat Genet.* 1995;11(1):64–70.
15. Edelmann W, Yang K, Umar A, Heyer J, Lau K, Fan K, et al. Mutation in the mismatch repair gene Msh6 causes cancer susceptibility. *Cell.* 1997;91(4):467–77.
16. Das A, Sudhaman S, Morgenstern D, Coblentz A, Chung J, Stone SC, et al. Genomic predictors of response to PD-1 inhibition in children with germline DNA replication repair deficiency. *Nat Med.* 2022;28(1):125–35.
17. Richardson TE, Yokoda RT, Rashidipour O, Vij M, Snuderl M, Brem S, et al. Mismatch repair protein mutations in isocitrate dehydrogenase (IDH)-mutant astrocytoma and IDH-wild-type glioblastoma. *Neurooncol Adv.* 2023;5(1):vdad085.

18. Bhatt D, Sundaram RK, Lopez KSL, Lee T, Gueble SE, and Vasquez JC. Development of Syngeneic Murine Glioma Models with Somatic Mismatch Repair Deficiency to Study Therapeutic Responses to Alkylating Agents and Immunotherapy. *Curr Protoc.* 2025;5(2):e70097.
19. Lin K, Gueble SE, Sundaram RK, Huseman ED, Bindra RS, and Herzon SB. Mechanism-based design of agents that selectively target drug-resistant glioma. *Science.* 2022;377(6605):502–11.
20. Vasquez JC, Bindra RS, and Gueble SE. Novel Strategies for Improved Treatment of O6-Methylguanine-DNA Methyltransferase Promoter-Methylated Glioma. *Medical Research Archives.* 2025;13(9).
21. Consortium APG. AACR Project GENIE: Powering Precision Medicine through an International Consortium. *Cancer Discov.* 2017;7(8):818–31.
22. Cheng J, Novati G, Pan J, Bycroft C, Zemgulyte A, Applebaum T, et al. Accurate proteome-wide missense variant effect prediction with AlphaMissense. *Science.* 2023;381(6664):eadg7492.
23. Ross JL, Chen Z, Herting CJ, Grabovska Y, Szulzewsky F, Puigdelloses M, et al. Platelet-derived growth factor beta is a potent inflammatory driver in paediatric high-grade glioma. *Brain.* 2021;144(1):53–69.
24. Louis DN, Perry A, Wesseling P, Brat DJ, Cree IA, Figarella-Branger D, et al. The 2021 WHO Classification of Tumors of the Central Nervous System: a summary. *Neuro Oncol.* 2021;23(8):1231–51.
25. Modrich P, and Lahue R. Mismatch repair in replication fidelity, genetic recombination, and cancer biology. *Annu Rev Biochem.* 1996;65:101–33.
26. Kuraguchi M, Yang K, Wong E, Avdievich E, Fan K, Kolodner RD, et al. The distinct spectra of tumor-associated Apc mutations in mismatch repair-deficient Apc1638N mice define the roles of MSH3 and MSH6 in DNA repair and intestinal tumorigenesis. *Cancer Res.* 2001;61(21):7934–42.
27. Westcott PMK, Muyas F, Hauck H, Smith OC, Sacks NJ, Ely ZA, et al. Mismatch repair deficiency is not sufficient to elicit tumor immunogenicity. *Nat Genet.* 2023;55(10):1686–95.
28. Jia P, Yang X, Guo L, Liu B, Lin J, Liang H, et al. MSIsensor-pro: Fast, Accurate, and Matched-normal-sample-free Detection of Microsatellite Instability. *Genomics Proteomics Bioinformatics.* 2020;18(1):65–71.
29. Nebot-Bral L, Hollebecque A, Yurchenko AA, de Forceville L, Danjou M, Jouniaux JM, et al. Overcoming resistance to alphaPD-1 of MMR-deficient tumors with high tumor-induced neutrophils levels by combination of alphaCTLA-4 and alphaPD-1 blockers. *J Immunother Cancer.* 2022;10(7).
30. Mandal R, Samstein RM, Lee KW, Havel JJ, Wang H, Krishna C, et al. Genetic diversity of tumors with mismatch repair deficiency influences anti-PD-1 immunotherapy response. *Science.* 2019;364(6439):485–91.
31. Li HD, Lu C, Zhang H, Hu Q, Zhang J, Cuevas IC, et al. A PoleP286R mouse model of endometrial cancer recapitulates high mutational burden and immunotherapy response. *JCI Insight.* 2020;5(14).
32. Neftel C, Laffy J, Filbin MG, Hara T, Shore ME, Rahme GJ, et al. An Integrative Model of Cellular States, Plasticity, and Genetics for Glioblastoma. *Cell.* 2019;178(4):835–49 e21.
33. Chen Z, Giotti B, Kaluzova M, Vallcorba MP, Rawat K, Price G, et al. A paracrine circuit of IL-1beta/IL-1R1 between myeloid and tumor cells drives genotype-dependent glioblastoma progression. *J Clin Invest.* 2023;133(22).
34. Ross JL, Puigdelloses-Vallcorba M, Pinero G, Soni N, Thomason W, DeSisto J, et al. Microglia and monocyte-derived macrophages drive progression of pediatric high-grade

gliomas and are transcriptionally shaped by histone mutations. *Immunity.* 2024;57(11):2669–87 e6.

35. Nduom EK, Wei J, Yaghi NK, Huang N, Kong LY, Gabrusiewicz K, et al. PD-L1 expression and prognostic impact in glioblastoma. *Neuro Oncol.* 2016;18(2):195–205.
36. Chen Z, Herting CJ, Ross JL, Gabanic B, Puigdelloses Vallcorba M, Szulzewsky F, et al. Genetic driver mutations introduced in identical cell-of-origin in murine glioblastoma reveal distinct immune landscapes but similar response to checkpoint blockade. *Glia.* 2020;68(10):2148–66.
37. Friebel E, Kapolou K, Unger S, Nunez NG, Utz S, Rushing EJ, et al. Single-Cell Mapping of Human Brain Cancer Reveals Tumor-Specific Instruction of Tissue-Invading Leukocytes. *Cell.* 2020;181(7):1626–42 e20.
38. Arrieta VA, Dmello C, McGrail DJ, Brat DJ, Lee-Chang C, Heimberger AB, et al. Immune checkpoint blockade in glioblastoma: from tumor heterogeneity to personalized treatment. *J Clin Invest.* 2023;133(2).
39. Kucherlapati MH, Lee K, Nguyen AA, Clark AB, Hou H, Jr., Rosulek A, et al. An Msh2 conditional knockout mouse for studying intestinal cancer and testing anticancer agents. *Gastroenterology.* 2010;138(3):993–1002 e1.
40. Marino S, Vooijs M, van Der Gulden H, Jonkers J, and Berns A. Induction of medulloblastomas in p53-null mutant mice by somatic inactivation of Rb in the external granular layer cells of the cerebellum. *Genes Dev.* 2000;14(8):994–1004.
41. Friedman HS, McLendon RE, Kerby T, Dugan M, Bigner SH, Henry AJ, et al. DNA mismatch repair and O6-alkylguanine-DNA alkyltransferase analysis and response to Temodal in newly diagnosed malignant glioma. *J Clin Oncol.* 1998;16(12):3851–7.
42. Chen Z, Soni N, Pinero G, Giotti B, Eddins DJ, Lindblad KE, et al. Monocyte depletion enhances neutrophil influx and proneural to mesenchymal transition in glioblastoma. *Nat Commun.* 2023;14(1):1839.
43. Huseman ED, Lo A, Fedorova O, Elia JL, Gueble SE, Lin K, et al. Mechanism of Action of KL-50, a Candidate Imidazotetrazine for the Treatment of Drug-Resistant Brain Cancers. *J Am Chem Soc.* 2024.
44. McCord M, Bartom E, Burdett K, Baran A, Eckerdt FD, Balyasnikova IV, et al. Modeling Therapy-Driven Evolution of Glioblastoma with Patient-Derived Xenografts. *Cancers (Basel).* 2022;14(22).
45. McCord M, Sears T, Wang W, Chaliparambil R, An S, Sarkaria J, et al. The novel DNA cross-linking agent KL-50 is active against patient-derived models of new and recurrent post-temozolomide mismatch repair-deficient glioblastoma. *Neuro Oncol.* 2024.
46. McFaline-Figueroa JL, Braun CJ, Stanciu M, Nagel ZD, Mazzucato P, Sangaraju D, et al. Minor Changes in Expression of the Mismatch Repair Protein MSH2 Exert a Major Impact on Glioblastoma Response to Temozolomide. *Cancer Res.* 2015;75(15):3127–38.
47. Friedmann-Morvinski D, and Hambardzumyan D. Monocyte-neutrophil entanglement in glioblastoma. *J Clin Invest.* 2023;133(1).
48. Stupp R, Mason WP, van den Bent MJ, Weller M, Fisher B, Taphoorn MJ, et al. Radiotherapy plus concomitant and adjuvant temozolomide for glioblastoma. *N Engl J Med.* 2005;352(10):987–96.
49. Le Rhun E, Oppong FB, Vanlancker M, Stupp R, Nabors B, Chinot O, et al. Prognostic significance of therapy-induced myelosuppression in newly diagnosed glioblastoma. *Neuro Oncol.* 2022;24(9):1533–45.
50. Saeed AM, Bentzen SM, Ahmad H, Pham L, Woodworth GF, and Mishra MV. Systematic review and pooled analysis of the impact of treatment-induced lymphopenia on survival of glioblastoma patients. *Radiat Oncol.* 2024;19(1):36.

51. Di Ianni N, Maffezzini M, Eoli M, and Pellegatta S. Revisiting the Immunological Aspects of Temozolomide Considering the Genetic Landscape and the Immune Microenvironment Composition of Glioblastoma. *Front Oncol.* 2021;11:747690.
52. Herting CJ, Chen Z, Maximov V, Duffy A, Szulzewsky F, Shayakhmetov DM, et al. Tumour-associated macrophage-derived interleukin-1 mediates glioblastoma-associated cerebral oedema. *Brain.* 2019;142(12):3834–51.

Figures

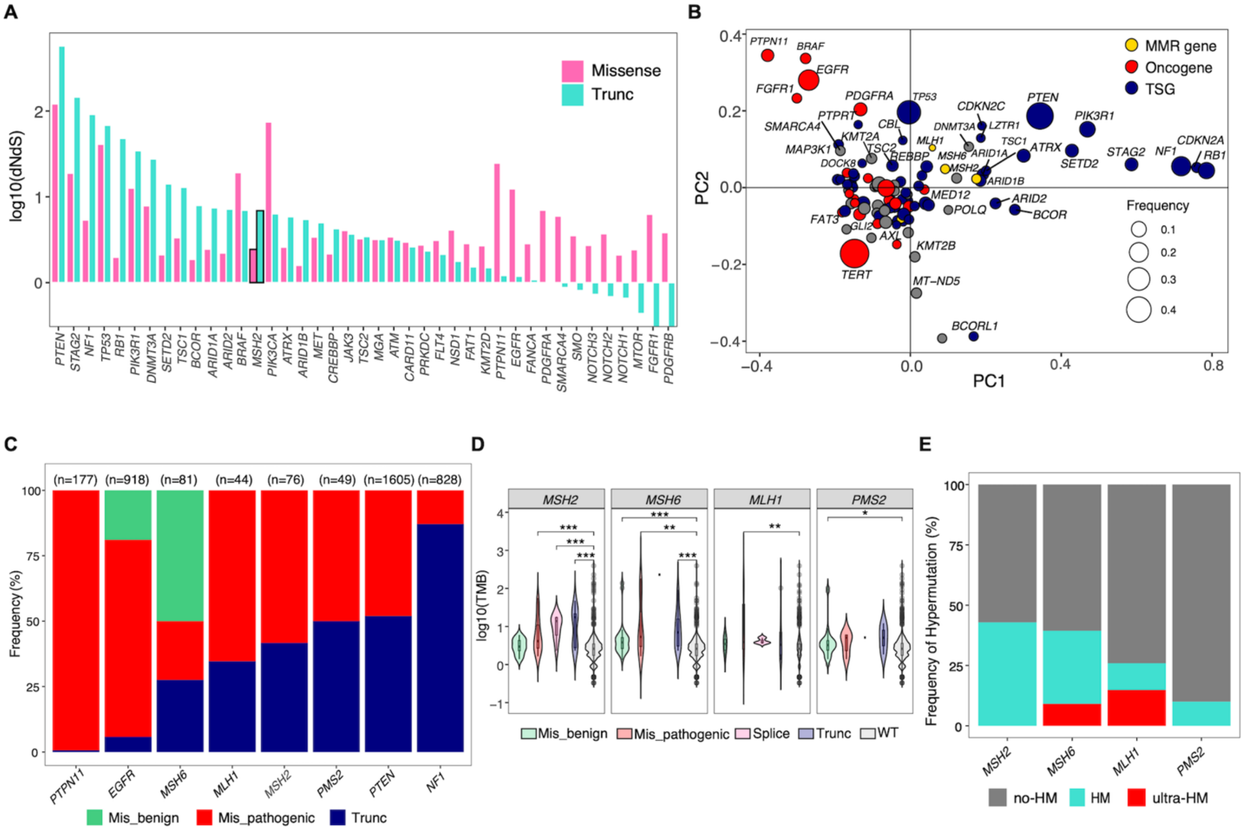

Figure 1. Distinct distributions of mutation types and correlations with tumor mutational burden highlight the functional divergence of MMR genes in GBM. (A) Positive selection of frequently-altered genes in GBM tumors. (**B)** Principal component analysis of frequently-altered genes in the GBM cohort based on mutation type representation. **(C)** Proportions of mutation types for each gene. **(D)** Comparison of TMB according to mutation type for each MMR gene. (**E)** Proportion of the HM phenotype in GBMs with MMR gene mutations. The Kruskal-Wallis test was used, followed by pairwise Wilcoxon rank-sum tests for post-hoc analysis. P-values were adjusted for multiple comparisons using the Bonferroni method for **D**. *p<0.05, **p<0.01, ***p<0.001, ****p<0.0001.

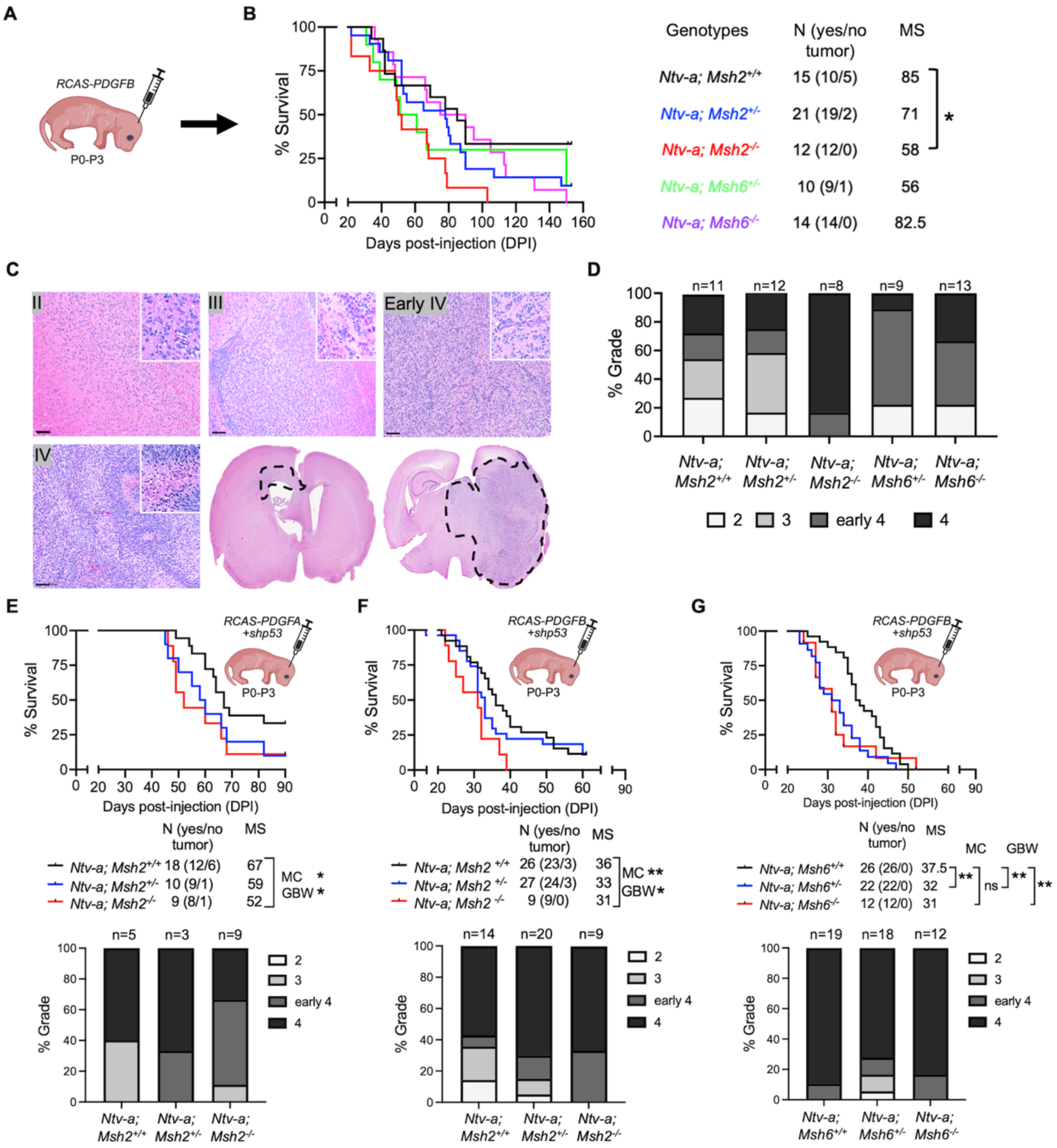

Figure 2. *Msh2* germline loss drives low-grade to high-grade glioma progression. (A) Schematic illustration of the generation of gliomas using overexpression of PDGFB in newborn mice. **(B)** Kaplan-Meier survival curves and corresponding median survival (MS) for various genotypes. (**C**) Corresponding H&E-stained tumors of various grades, and (**D**) distribution of various grade tumors in different genotypes. Survival curves and corresponding quantification graphs of tumor grade for *PDGFA+shp53* tumors in **(E)**, *PDGFB+shp53* in **(F)** in *Ntv-a; WT*, *Ntv-a; Msh2*$^{+/-}$, and *Ntv-a; Msh2*$^{-/-}$ genotypes and **(G)** *PDGFB+shp53* in *Ntv-a; WT*, *Ntv-a; Msh6*$^{+/-}$, and *Ntv-a; Msh6*$^{-/-}$ genotypes. Log-rank (Mantel-Cox - MC) and Gehan-Breslow-Wilcoxon (GBW) test for **B, E-G**. *$p<0.05$, **$p<0.01$.

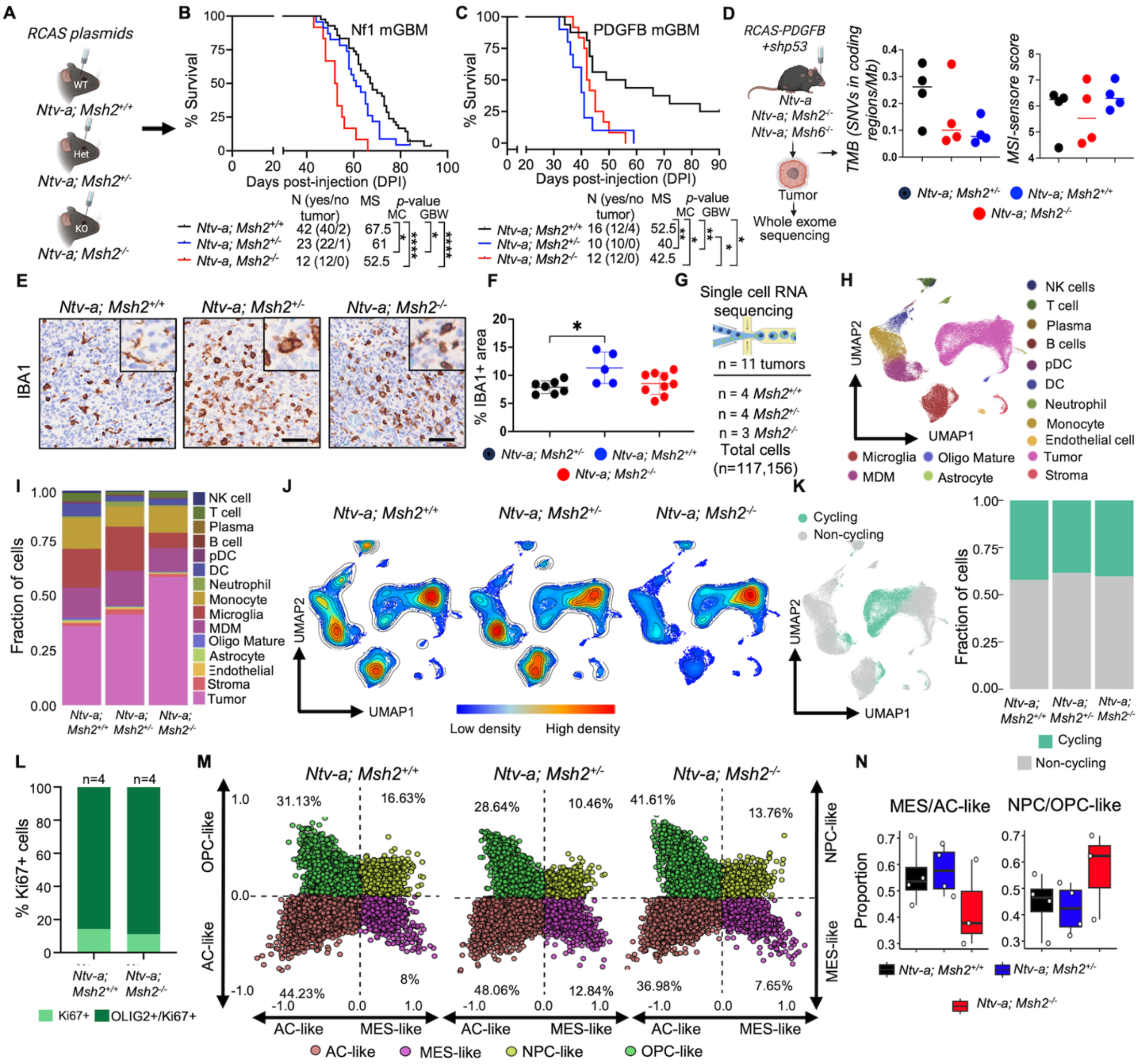

Figure 3. Germline loss of *Msh2* drives GBM progression in adult mice without increasing TMB and MSI. (A) Schematic illustration for the generation of adult mGBM models and **(B)** Kaplan-Meier survival curves of Nf1 mGBM and **C)** PDGFB mGBM. **(D)** Schematic illustration of the experiment for WES. Data are presented as SNV in coding regions per Mb of sequenced DNA, and MSI scores from WT, Msh2, and Msh6-deficient tumors. **(E)** Representative images and **(F)** quantification of IHC for IBA1+ TAMs in tumors from **C**. **(G)** Overview of sample processing for scRNA-seq. **(H)** Uniform Manifold Approximation and Projection (UMAP) plot for all non-immune and immune cell scRNA-seq data in this study, colored by cell type annotation. **(I)** Stacked bar plots depicting the proportion of annotated cells within various genotypes. **(J)** UMAP plots of all cells colored by cell density, where red indicates high cell density and blue indicates low density. **(K)** UMAP plots of cells colored by cell cycle status and stacked bar plots depicting the proportion of annotated cells within various genotypes. **(L)** Quantification graph of multiplex IF for Ki67 and OLIG2 double-positive cells in Ki67+positive population from tumors. **(M)** Two-dimensional quadrant scatter plot representing the GBM cellular state across tumor cells split by *Msh2* status, where orange color indicates the AC-like, purple color indicates the MES-like, yellow indicates the NPC-like, and green indicates the OPC-like (32). **(N)** Sum of average MES- and AC-like scores (left) and sum of average NPC- and OPC-like scores (right) across

samples split by *Msh2* genotypes, with t-test *P* values calculated; black= *WT,* blue = *Msh2 HET,* and red = *Msh2 KO*. MC and GBW test for **B**. One-way ANOVA followed by Tukey's *post hoc* analysis for **F**. *p<0.05, **p<0.01. Scale bar = 100 µm, scale bar in inset = 50 µm.

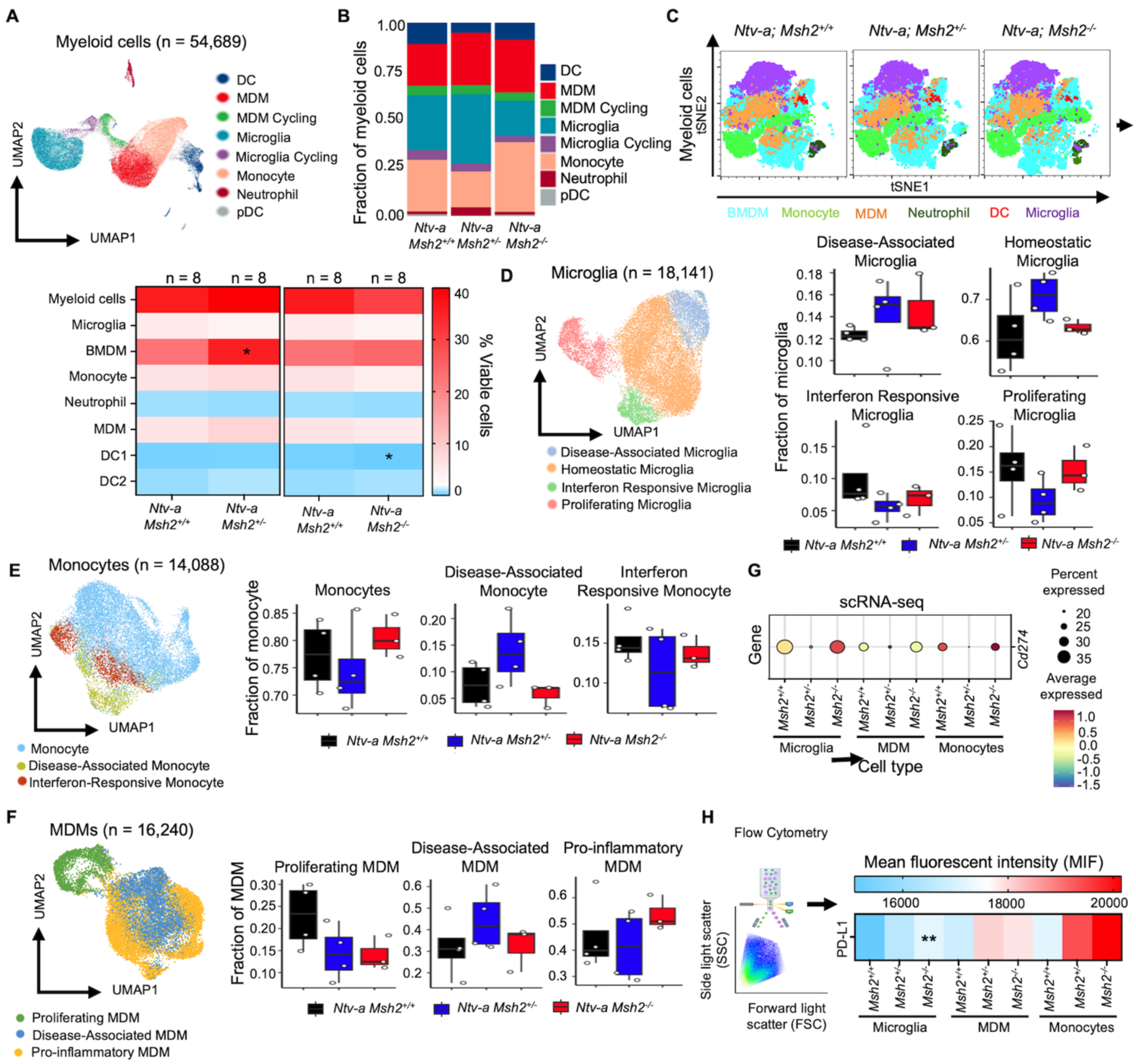

Figure 4. Disease-associated myeloid subsets are increased in *Msh2*-dependent MMR-reduced and MMR-deficient tumors. (A) UMAP plot of all sequenced mGBM myeloid cells, colored by annotated myeloid cell subset. **(B)** Stacked bar plots depicting the proportion of annotated myeloid cell subsets. **(C)** tSNE plots showing results of spectral flow cytometry of myeloid panel in the tumors (upper right) and heatmaps representing quantification (bottom left). (**D)** UMAP plot of all mGBM microglia cells from the scRNA sequencing dataset colored by annotated microglia subsets. Distribution of microglia subset proportions, split by *Msh2* status, black= *WT*, blue = *Msh2 HET,* and red = *Msh2 KO*. **(E)** Left: UMAP plot of all mGBM monocytes colored by annotated monocytes subsets. Right: Distribution of monocyte subset proportions, split by *Msh2* status, black= *WT*, blue = *Msh2 HET,* and red = *Msh2 KO*. (**F**) Left: UMAP plot of all mGBM MDM colored by annotated MDM subsets. Right: Distribution of MDM subset proportions, split by *Msh2* status, black= *WT*, blue = *Msh2 HET,* and red = *Msh2 KO*. **(G)** Dot plot showing expression levels and the percentage of cells expressing *Cd274* gene for each annotated myeloid cell subset based upon *Msh2* status. **(H)** Schematic illustration of flow cytometry and heatmap quantification of PD-L1 expression in different myeloid cell populations based on *Msh2* status. One-way ANOVA followed by Tukey's *post hoc* analysis for **C** and **H**. *p<0.05, **p<0.01.

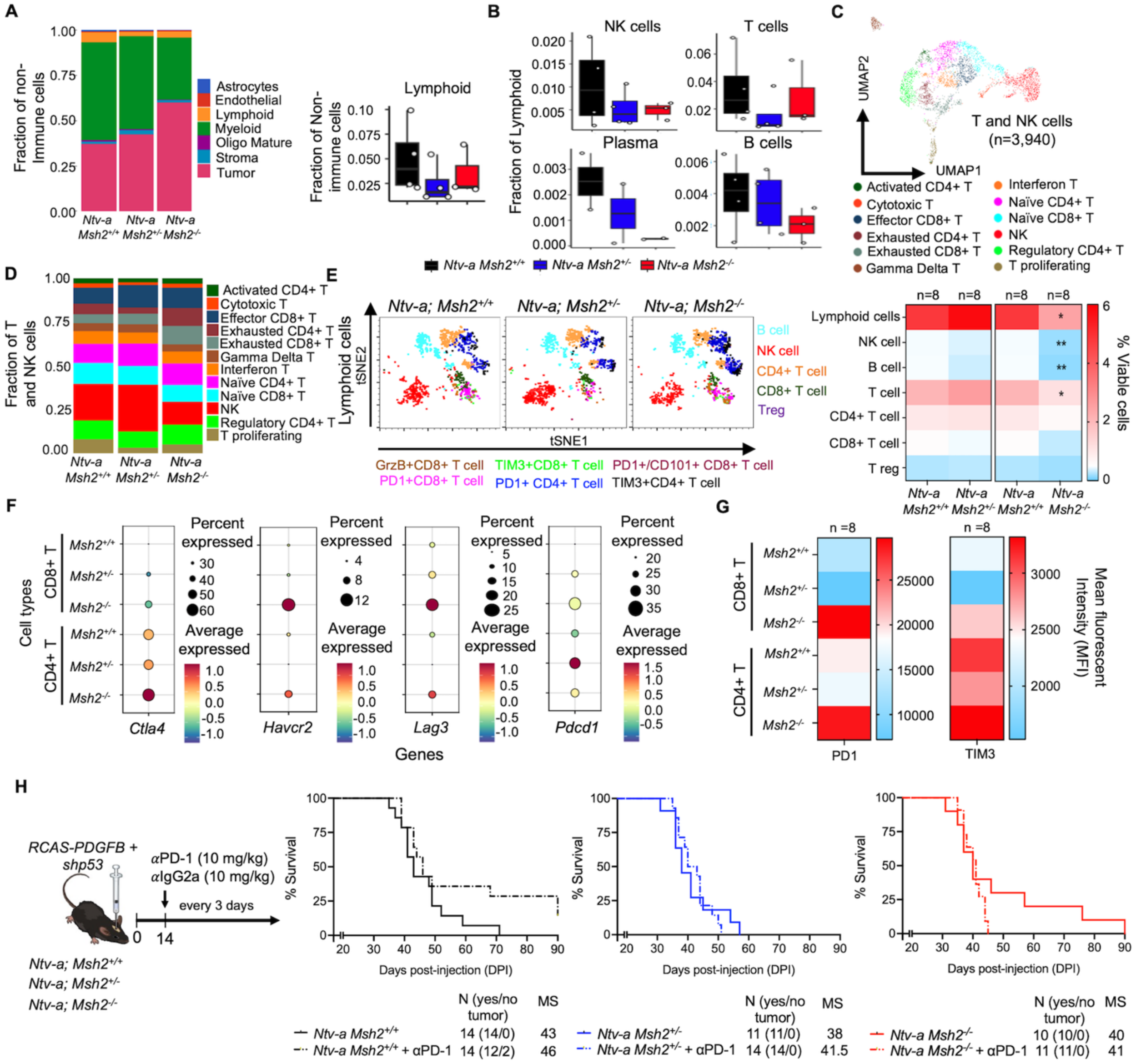

Figure 5. Germline *Msh2* loss-driven MMR-deficient tumors exhibit reduced lymphoid infiltration and increased exhaustion of CD8+ T cells but show no response to ICI. (A) Left: Stacked bar plots depicting the proportion of non-immune and immune cell subsets based upon *Msh2* status. Right: Box plot showing the distribution of the proportion of lymphoid fraction based upon *Msh2* status. **(B)** Distribution of NK, T, plasma, and B cell proportions relative to all cells (see Figure 2G). (**C**) UMAP plot of all sequenced mGBM T and NK cells, colored by cell subset annotations. **(D)** Stacked bar plots depicting the proportions of various T and NK cell subsets based upon the *Msh2* status of tumors. (**E**) Schematic illustration of flow cytometry and heatmaps of quantifications of lymphoid cell populations. (**F**) Dot plot showing expression levels and the percentage of cells expressing genes encoding immune checkpoint proteins across CD8 and CD4 T cells split by *Msh2* genotypes. **(G)** Heatmap quantification of PD-1 and TIM3 mean fluorescent intensity in CD8+ and CD4+ T cells from various tumor genotypes. (**H**) Schematic illustration of experimental steps for αPD-1 treatment and corresponding Kaplan-Meier survival curves of *WT*, *Msh2*$^{+/-}$ and *Msh2*$^{-/-}$ mice injected with *PDGFB+shp53* treated with αPD-1 or isotype control - αIgG2a. MC and GBW test for **H**, One-way ANOVA followed by Tukey's *post hoc* analysis for E.*p<0.05, **p<0.01.

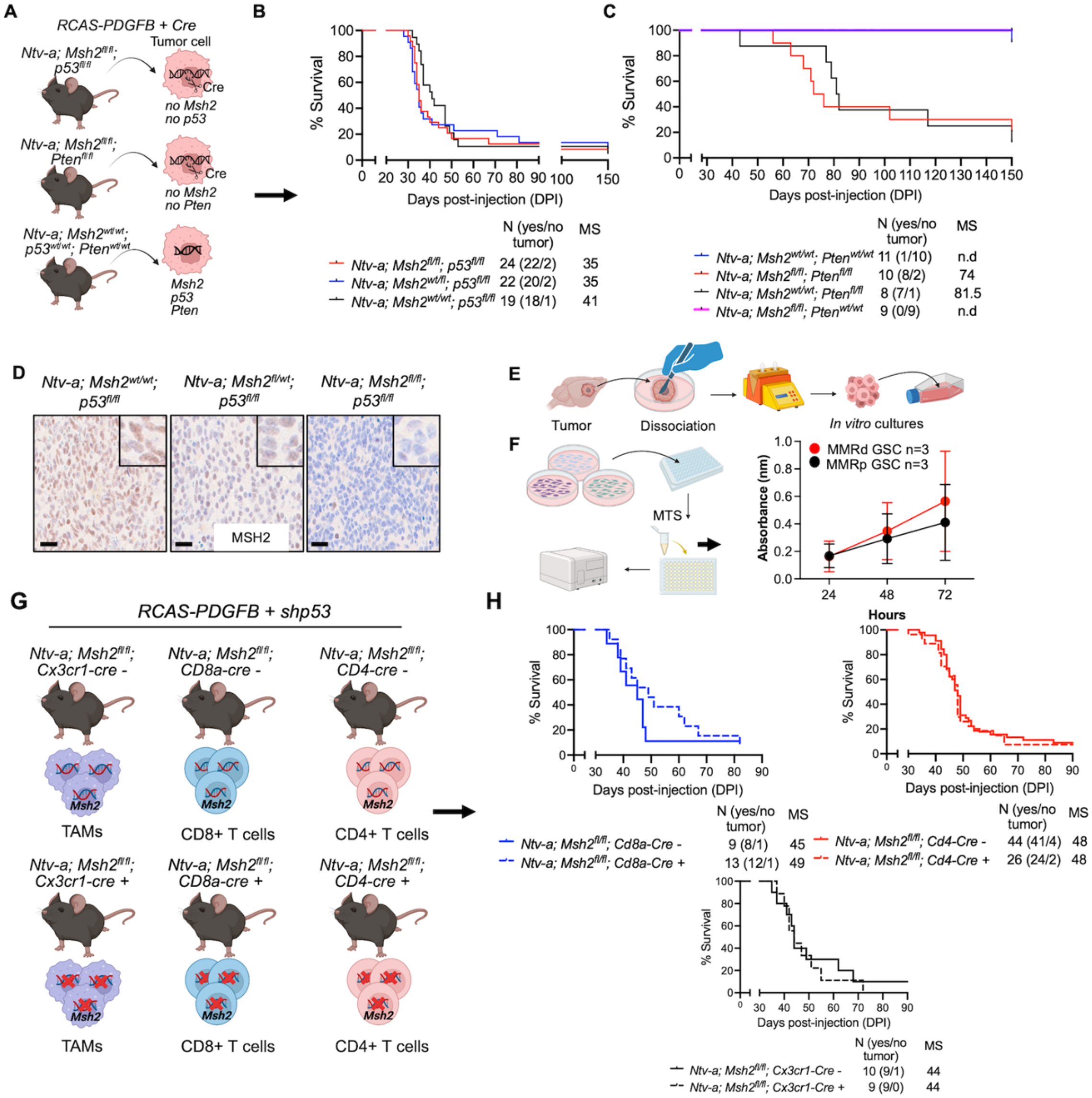

Figure 6. Somatic MMRd does not confer shortened survival in tumor-bearing mice. (A) Schematic illustration for the generation of adult somatic *Msh2* loss-induced MMR-deficient GBM models utilizing PDGFB overexpression along with either *shp53 or shPten* across various genotypes**.** (**B** - **C**) Kaplan-Meier survival curves of tumors in various genotypes. (**D)** Representative images and quantification of IHC for MSH2 in somatic homozygous or heterozygous MMRd tumors. (**E)** Illustration of the isolation and culture of freshly-dissociated primary tumors generated in germline *Msh2, WT,* and *Msh2*-deficient mice. (**F)** Illustration of the experimental setup and results for the MTS assay for MMRp and MMRd primary tumor cell cultures maintained in GSC conditions. The experiments included three replicates for each genotype, with primary cell lines derived from three different tumor-bearing mice. Experiments were repeated at least three times for each line at 24hr, 48hr, and 72hrs. (**G)** Schematic illustration showing generation of adult *Msh2*-cell specific depletion GBM models utilizing PDGFB overexpression combined with *shp53* across different genotypes. **(H)** Kaplan-Meier survival curves of tumors in various genotypes. The experiments included three replicates for each genotype, with primary cell lines derived from three different tumor-bearing mice. Experiments were repeated at least three times for each line at 24hr, 48hr, and 72hrs. MC and GBW test for **B**, **C** and **H**. Scale bar = 100 µm, scale bar in inset = 50 µm for **C**.

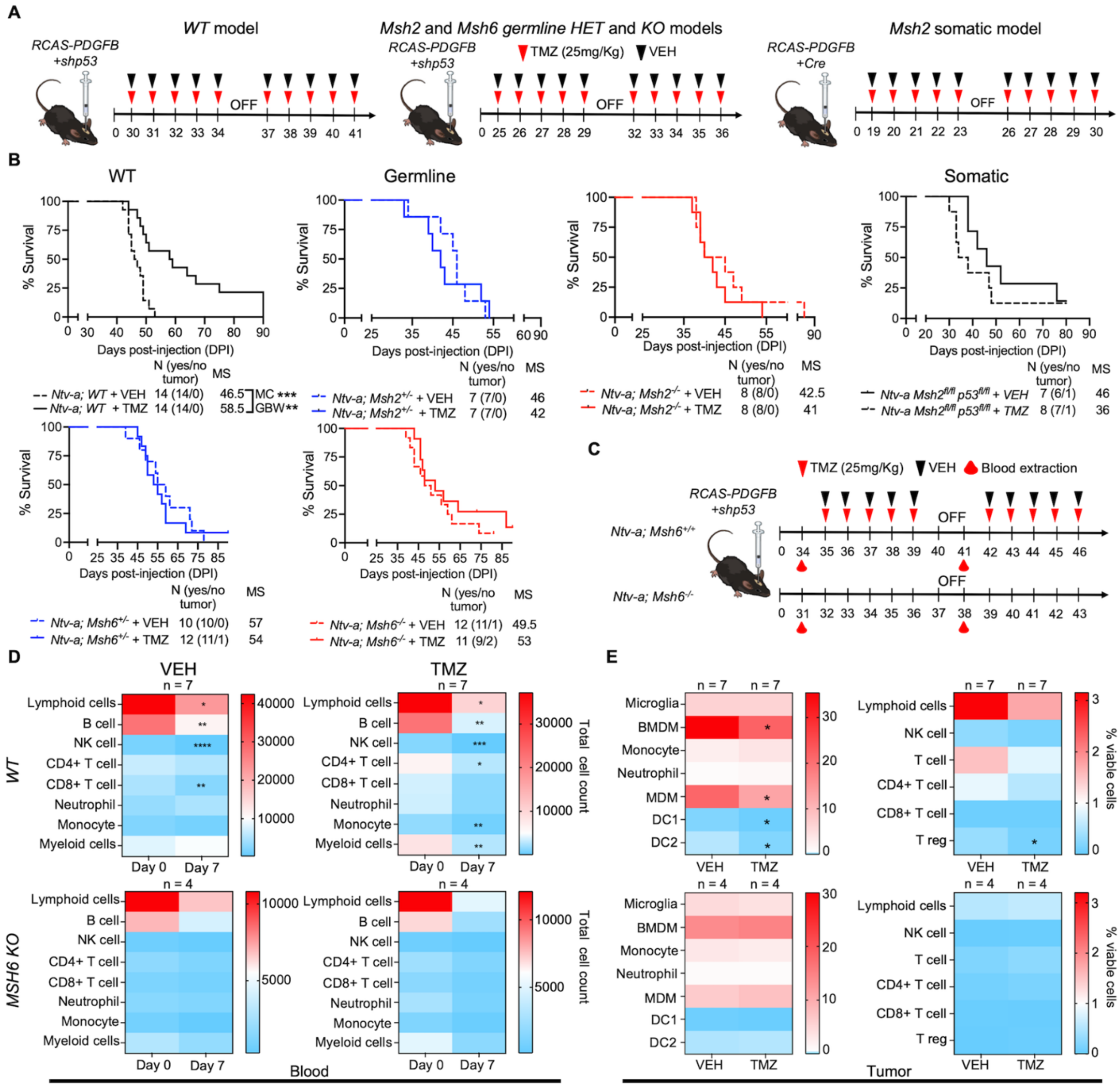

Figure 7. Germline MMR-reduction, MMR-deficiency and somatic MMR-deficiency confer resistance to TMZ *in vivo*. (**A**) Schematic illustration of experimental steps for TMZ treatment. (**B**) Survival curves of tumor-bearing mice treated with VEH or TMZ. (**C**) Schematic illustration of experimental steps for TMZ treatment and time points of blood and tumor collection. (**D**), Heatmap quantifications of spectral flow cytometry myeloid and lymphoid panels in the blood at days 0 and 7, (**D**) and tumors at the endpoint of survival (**E**). MC and GBW test for **B** and Student's *t*-test for **D** and **E**. *p<0.05, **p<0.01, ***p<0.001.

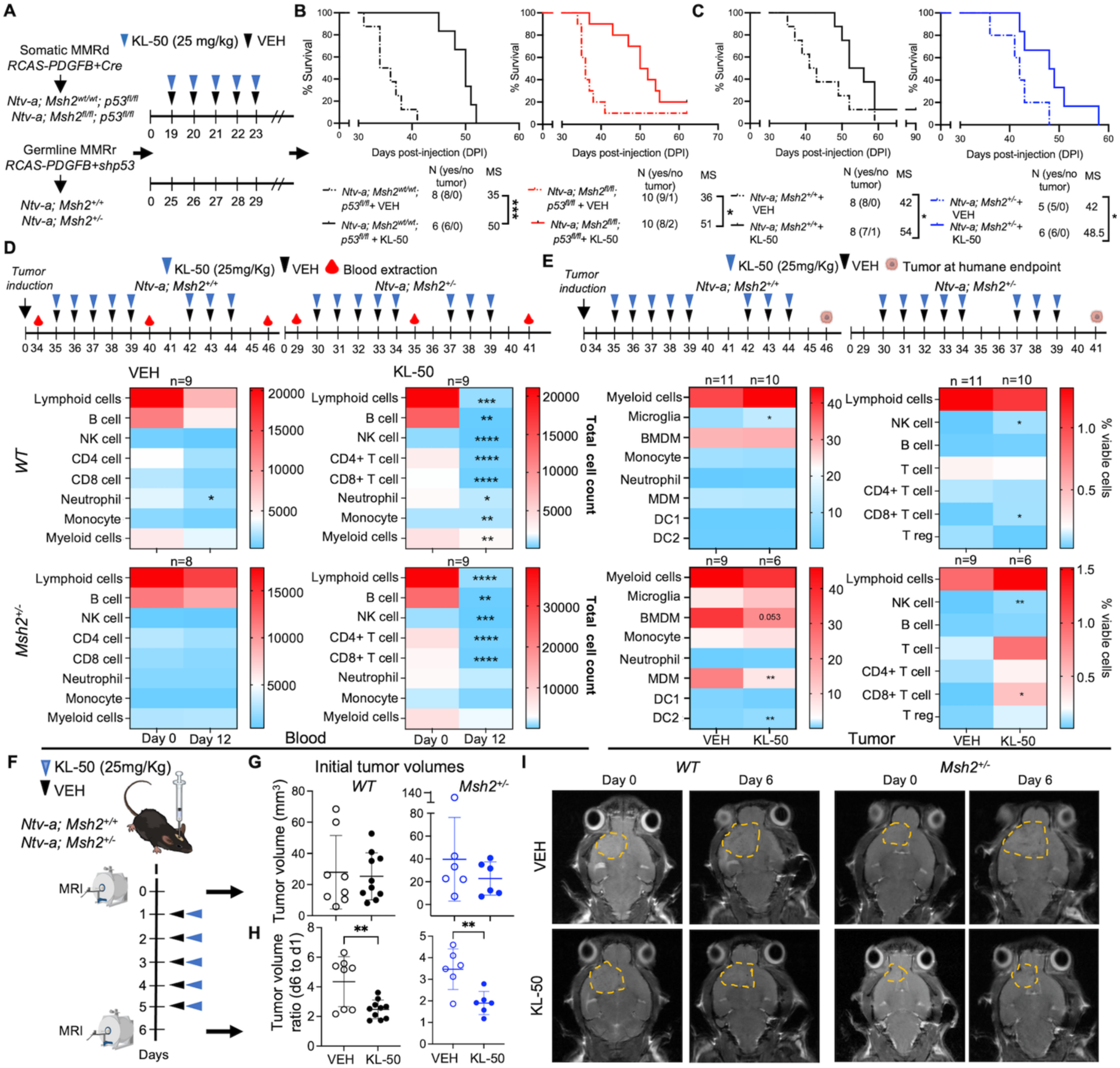

Figure 8. KL-50 treatment is potent against MMRp tumors as well as germline and somatic MMRd tumors. (A) Schematic illustration of experimental steps for KL-50 treatment in *WT* and somatic MMRd tumor-bearing mice and in *WT* and germline MMRd tumor-bearing mice. **(B)** Survival curves of *WT* and somatic MMRd tumor-bearing mice treated with VEH or KL-50. **(C)** Survival curves of *WT* and *Msh2* HET tumor-bearing mice treated with VEH or KL-50. **(D)** Schematic illustration of experimental steps for KL-50 treatment and time points of blood and Heat map quantifications of spectral flow cytometry myeloid and lymphoid panels in the blood at treatment days 0 and 12 and tumors at day 12 (48 hrs. after the last dose). **(E)** Schematic illustration of experimental steps for KL-50 treatment and time point of tumor collection and Heat map quantifications of spectral flow cytometry myeloid and lymphoid panels. **(F)** Schematic illustration of experimental steps for MRI-based assessment of KL-50 efficacy in germline MMRd tumor-bearing mice. **(G)** Initial MRI volumes equally distributed in VEH and KL-50 groups in WT and germline MMRd tumors. **(H)** Ratio of tumor volume at day 6 post-treatment over initial pre-treatment volumes. **(I)** Representative MRI images of WT and germline MMRd tumor-bearing mice at day 0 and day 6 post-VEH and KL-50 treatment. MC and GBW test for **B** and Student's *t*-test for **D-E**, **H-I**. *p<0.05, **p<0.01, ***p<0.001.